Development of a Robust Three-Dimensional Finite Element Method-Based Model of a Micro-Ring Resonator for Biosensing

Timothy Jean Guy Perrier

Department of Electrical & Computer Engineering
McGill University
Montréal, Québec, Canada

July 4, 2023

A thesis submitted to McGill University for the degree of Master of Science - Electrical Engineering

Abstract

This thesis presents the development of a robust three-dimensional, finite element method (FEM) model of an add-drop micro-ring (ADMR) resonator to be used as a biosensor. The model was developed in a way that makes it easily scalable to any device size, only limited by computer system specifications. A customizable absorption coefficient can be added to materials to accurately reflect losses due to sidewall roughness. Various configurations are simulated and compared with experimentally measured rings and results from literature to confirm the accuracy of the model. Important coefficients describing the ADMR characteristics are extracted, and relationships between these coefficients and parameters were investigated to predict ring performance. The coefficients were also used to generate an analytical model to observe the free spectral range (FSR) of the device.

Results show that the simulated rings, as expected, perform better than the experimentally measured rings in terms of the quality factor (QF). The 5 μm radius ring in the TM mode has a simulated QF that is 7.78% larger than the most prominent QF of the measured ring. The FSR values extracted from the analytical models are accurate to a range of ± 1 nm in comparison to those of the measured rings. The simulated QF increases exponentially as the gap size increases, which corresponds to the relationship with the intrinsic QF explored in various studies. The computational complexity of the model is investigated to observe how the accuracy is affected as a result of changing the mesh quality.

Abrégé

Cette thèse présente le développement d'un modèle de méthode des éléments finis (MEF) robuste et tri-dimensionnel d'un micro-résonateur annulaire photonique pour être utilisé comme biocapteur. Le modèle MEF 3d a été conçu de façon à être flexible pour n'importe quelle configuration, limité seulement par les performances de l'ordinateur. Un coefficient d'absorption peut être ajouté aux matériaux pour simuler la rugosité des parois du guide d'onde. Pour confirmer la précision du modèle, des comparaisons sont faites entre les résultats de ces simulations, des résultats mesurés, et des résultats de littérature. Plusieurs coefficients importants, qui décrivent les caractéristiques du résonateur, sont calculés. Les relations entre ces coefficients et les paramètres du résonateur ont été examinées pour prédire la performance du résonateur. Les coefficients ont aussi été utilisés pour produire un modèle mathématique permettant d'observer la plage spectrale libre (PSL).

Les résultats montrent que la performance des simulations est meilleure que celle des résonateurs mesurés du point de vue du facteur de qualité (FQ). Le FQ simulé du résonateur avec un rayon de 5 μm en mode de polarisation TM est 7,78% supérieur au FQ du résonateur mesuré. Le FQ simulé augmente exponentiellement avec la distance entre les guides d'onde. Ce résultat correspond au rapport avec le FQ intrinsèque qui a été examiné dans plusieurs études. Les valeurs de la PSL dérivées du modèle mathématique sont précises à $\pm$ 1 nm par rapport á celles des résonateurs mesurés. La complexité algorithmique du modèle a été évaluée pour observer la précision des résultats obtenus par rapport à la variance du maillage.

Acknowledgements

I would like to begin thanking my supervisor, Prof. Andrew Kirk, for introducing me to this field and project, and for guiding and supporting me throughout the process. Thank you Prof. Odile Liboiron-Ladouceur as well for allowing me to explore the topics I was interested in before suggesting that I switch to Prof. Kirk's group.

Thank you to all the students in the group for the help throughout my research and time spent here. Mohammad Motavas acted as an amazing mentor, helping to explain certain concepts, providing lots of insight, and teaching me how to perform measurements of the ring resonators in the lab.

I'd like to thank some of my friends, Juan and Martin, who kept me entertained throughout my studies. Je voudrais aussi remercier mes amis de famille, Geneviève et Gaby, qui m'ont aidé à m'intégrer à Montréal pendant la crise de COVID. Merci aussi pour toujours être prêt à me recevoir sans souci.

Finalement, je voudrais remercier ma famille pour leur amour et support inconditionnel. Je voudrais commencer avec mes parents, Arnaud et Delphine Perrier, pour leur support éternel et pour toujours croire en moi - surtout pendant le début de mes études. Merci à ma soeur, Brittany, pour les photos de ses crazy dogs, et pour être la meilleure soeur possible (même si ont ne se parle pas assez). Merci à mes grands-parents, Moutick, Tad, Papy, et Mamy, pour votre support - même si je n'appelle pas autant que vous voudriez.

Contents

List of Figures

List of Tables

List of Acronyms

ADMR Add-Drop Ring Resonator.

APMR All-Pass Ring Resonator.

BMA Boundary Mode Analysis.

CMOS complementary metal–oxide–semiconductor.

CPU Central Processing Unit.

DC directional coupler.

FDTD Finite Difference Time Domain.

FEM Finite Element Method.

FSR free spectral range.

FWHM full width at half maximum.

GPU Graphics Processing Unit.

MRR Micro-Ring Resonator.

MZI Mach-Zehnder interferometer.

ORR optical ring resonator.

POC Point of Care.

QF quality factor.

SIPH Silicon Photonic.

SNR Signal to Noise Ratio.

SOI silicon on insulator.

TE Transverse Electric.

TM Transverse Magnetic.

Chapter 1

Introduction

1.1 History and Present Challenges

The development of biosensors dates back to the early 1900s when scientists developed devices to measure acid concentration in liquids, which was soon followed by defining pH and the ability to measure it [2]. However, it would not be before 1956 that the first modern biosensor would be developed to detect oxygen using an electrode. Shortly after in 1962, Leland Clark would also demonstrate the ability to detect glucose using an amperometric enzyme electrode [2]. This discovery eventually led into a cascade of development of ”modern” biosensors.

Traditionally, testing has been done in off-site medical laboratories, which requires significantly more processing time. Point-of-care (POC) testing occurs in a clinical setting, and is performed by a trained professional. Typically, it can be done without having a patient wait for hours or days to receive results. Today, popular POC devices currently include oximetry, continuous glucose monitoring systems, and test strips for both pregnancy testing and glucose monitoring. The market has seen increasing demand for rapid POC systems to monitor various new biomarkers; however, the biosensing ecosystem has yet to mature enough to be ready for large scale implementation in clinical settings. Presently, a big issue in detecting analytes is the sensitivity of these biosensors. In cancer monitoring for example, important biomarkers such as EGFR and SOD3 can appear in concentrations down to the order of ng/mL [3]. Most commercial POC biosensors also lack the ability for multiplexing, which would provide much more information due to being able to detect multiple analytes simulatneously.

A relatively recent development in the biosensing field is the emergence of silicon photonic (SIPH) devices. The fabrication process for these sensors is compatible with modern SOI and CMOS technology, making them easy to produce and an attractive alternative to conventional biosenors.

Modeling SIPH devices such as micro-ring resonators (MRRs) in 3D is a challenge due to the complex nature of the math and physics surrounding them. The complexity of these devices causes the need for heavy computational power if robust simulations are desired for accurate predictions of the system.

A simple, preliminary approach that has been common in the past is the use of 2D simulations for devices such as MRRs. These can be split into two main categories: cross-sectional simulations focused on the waveguide mode profile and top-down simulations of the whole system. Although they are very accurate, cross-sectional simulations can only be used to determine mode profiles. A study by Bahadori et al. contains an excellent example of using a FEM-based cross-sectional simulation to determine mode profiles in two regions of a MRR [4]. On the other hand, 2D top-down simulations are very efficient, but the structure thickness must be approximated as an infinite slab. This causes major inaccuracies in the propagated mode that are far from the results obtained in a cross-sectional mode profile. These top-down 2D simulations also lack the ability to model the medium above and below the waveguide core such as having an oxide substrate with water above.

The two most common simulation types in this domain are the Finite-Difference-Time-Domain (FDTD) and the Finite Element Method (FEM). FDTD is a very common method for solving electromagnetic problems with a time-dependence. On the other hand, FEM works in steady-state, or in the frequency domain [5]. With both FDTD and FEM, distinct TE and TM modes of the waveguide core with accurate effective mode index (n_{eff}) values can be studied. These modes can then be propagated throughout a structure with great accuracy. A big advantage to 3D FEM is the flexibility of use with other physics problems such as heat transfer, fluid dynamics, and surface chemistry to simulate much more robust models.

1.2 Research Objectives

This thesis is aimed at providing an accurate 3D model for the design of optical MRRs using the Finite Element Method (FEM). The model can be used for detection of biological substances thanks to the ability to model various media above the resonator. The models were developed and simulated in COMSOL Multiphysics, and analytical models along with experimental measurements were also used to validate simulation results. Boundary mode analyses from the 3D model are compared to 2D cross-sectional simulations for validation. Following preliminary simulations and analysis, optimization was performed to find the best waveguide and ring parameters for a combination of good quality and performance. The optimization explores the effects that various parameters have on the performance of the MRR. Parameters tested include the coupling gap size, radius, and the use of TE and TM modes.

Chapter 2

Literature Review

2.1 Biosensors

A biosensor is a device that incorporates a bio-recognition element to produce a measurable signal caused by a binding event through the use of a transducer [6]. The major applications for biosensors are drug discovery, disease detection, environmental monitoring, soil quality monitoring, food quality monitoring, water quality management, toxins of defense interest, and prosthetic devices [2, 7]. Biosensors consist of five main components which can be seen in Figure 2.1: the analyte, bioreceptor, transducer, electronics, and display [2].

The analyte is the substance of interest to be detected using a biosensor. Analytes can consist of anything from bacteria to molecules such as glucose or contaminants such as heavy metals (mercury, lead, etc.). Bioreceptors are biological components that are used to detect

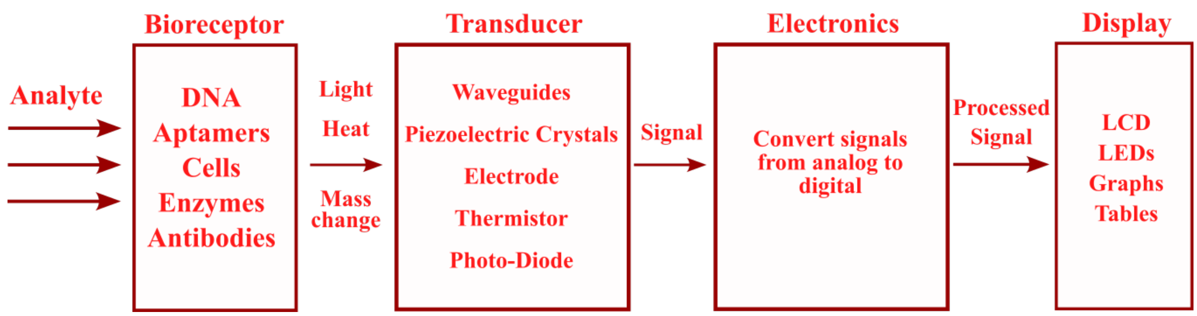

Figure 2.1: Diagram showing each part of a biosensor and how they relate to each other.

the specific analyte of interest. They can be in the form of DNA, Aptamers, whole cells, enzymes, and antibodies to list a few. The transducer of a biosensor is the component that converts energy from a binding event into an analog signal. This analog signal is then processed by the electronics, and the data can be displayed to the user. This can come in the form of an LCD, LEDs, graphs, numbers, and more.

The performance of biosensors can be evaluated using two main metrics: selectivity and sensitivity.

The specificity of a biosensor describes the ability of the biosensor to differentiate between the target analyte and everything else [8–10]. This metric is extremely important as the higher the specificity is, the lower the false positive rate will be. Different biorecognition elements have various affinities to specific types of analytes.

The sensitivity of a biosensor is defined as the relationship between the signal intensity and the changing concentration of the target analyte [10]. This comes in the form of the gradient of the signal response curve as a function of the changing analyte concentration [11]. Highly sensitive biosensors generate a quantifiable response based on a very small change in analyte concentration. The upper and lower limits of detection (LoD) can be used to describe the sensitivity. Ideally, this range should reflect the relevant physiological concentration range of the target analyte [10]. The dynamic range is the measurable range of analyte concentrations. Typically, the dynamic range follows a logarithmic curve and saturates after a certain concentration [11]. This saturation occurs when there is no more space left for analytes to bind to the bioreceptors. Usually, sensitivity is determined by the amount of surface area available for bioreceptors - the more binding sites available, the higher the sensitivity of the device [10]. The sensitivity is also heavily impacted by the type of biorecognition element used. For example, aptamers, which are smaller than antibodies, offer a larger sensitivity due to the ability to fit more of them over a given surface area [10].

In the case of MRR-based biosensors, the main aspects to focus on optimizing are the quality factor (QF) and the signal-to-noise ratio (SNR). Both of these metrics can vary based on ring radius, waveguide dimensions, TE/TM mode propagation, wavelength, and coupling gap. Since MRR-based results rely on shifts in resonance wavelength, having a high QF helps with the ability to distinguish resonance peaks. Typically, the TE mode yields higher QF values due to the mode being more confined in the waveguide [12]; however, it is less sensitive to RI changes in the surrounding medium caused by binding events. This is explored in a study by Cheema et al., confirming that as the mode expands further out due to reduced RI difference between the core and cladding, lossy media such as water cause an increase in loss, in turn, affecting the QF [13]. The SNR plays a major part in readability of results. Small

SNRs can cause confusion when observing transmission spectra as the noise may interfere with the resonance peaks.

2.2 Bioreceptors and Analytes

The core component of a biosensor is its bioreceptor, which is tailored to a specific analyte that is the target for detection. These bioreceptors can come in the form of antibodies, aptamers, enzymes, cells, DNA, or nanoparticles. Each of these bioreceptors have their own advantages and tradeoffs. When analytes bind to bioreceptors, the presence of the bound analyte can be detected in the form of refractive index (RI) changes, mass changes, or resistive changes to name a few. This is called the binding event.

Each biorecognition element comes with its own set of advantages and disadvantages. Antibodies and enzymes have great selectivity and re-usability; however, there can easily be batch variations and poor process stability. On the other hand, aptamers are very sensitive and have a low LOD, but they are expensive to produce and may not be as selective [10].

To detect any of these changes from the binding event, the bioreceptor must be bound to the transducer. This can be performed through surface functionalization. Main methods for this include covalent coupling to the biosensor's surface, covalent coupling to a polymer layer on the biosensor's surface, physical entrapment, and adsorption [14].

2.3 Surface Functionalization

When functionalizing the surface of a biosensor, the biorecognition elements must be immobilized while keeping it active. Physical, or reversible immobilization is a technique used that does not require any chemical bonding. These include physical adsorption and entrapment. A few examples of these are microencapsulation, electropolymerization, and using the sol-gel technique [15]. On the other hand, chemical, or irreversible immobilization, consists of generating strong chemical bonds between the surface of the transducer and the biorecognition elements. The two main methods are covalent bonding, being the most commonly used technique, and cross-linking [15]. Both of these methods result in much stronger bonds between the transducer and the biorecognition element in comparison to the physical immobilization techniques.

2.4 Conventional Detection Methods

Currently, nucleic acid amplification using the polymerase chain reaction (PCR) method is considered the gold standard for applications such as disease detection [16]. PCR is extremely accurate down to being able to differentiate specific serotypes of a virus [17]. Although the accuracy of PCR is close to unmatched, the equipment used is very expensive, and well-trained personnel are required to run diagnoses in dedicated laboratories [16]. Another disadvantage is that the process can take upwards of 150 minutes to complete [18,19], making it much slower than some novel approaches such as surface plasmon resonance which can take between 7 to 14 minutes [19–21]. This long time requirement does not include the time required to transport samples to dedicated laboratories [19]. Various kinds of immunoassays are another common approach for this field, and they are commercially available; however, the devices used to run these diagnostics are extremely expensive and are reserved for use in dedicated laboratories [19].

Enzyme linked immunosorbent assay (ELISA) sensors are the main competition to immunoassays, and they are widely used to detect foodborne pathogens such as Salmonella, and E. Coli [22]. They are also often considered the gold standard technique for biosensing thanks to their wide range of applications, ease of use, and scalability [23]. ELISA sensors offer multiple detection methods which include direct, indirect, and sandwich ELISA detection [24]. Typical ELISA sensors use colorimetry methods to detect substances [23, 24]. Although ELISA sensors are considered as the gold standard, they come with disadvantages which include cost per assay, time required for assay development, and the complex protocol to perform tests [25, 26]. Forming a conjugation between an enzyme and antibody requires incubation time [27].

The first commercially available biosensor was a glucose sensor for patients with diabetes [28]. Glucose monitoring systems remain the most common commercially available biosensors, notably due to their high accuracy and precision combined with ease of use [28]. These biosensors use electrochemical transducers which affect the re-usability of the sensor in the long-term due to gradual erosion of sensor reagents. This can cause erroneous measurements caused by carryover from previous results [29].

2.5 Silicon Photonic Biosensors

Thanks to the advanced and widely used SOI and CMOS fabrication processes, silicon photonic (SIPH) devices have begun to appear as an attractive alternative to conventional biosensing methods. In comparison to other types of transducers, SIPH-based biosensors offer advantages such as higher sensitivity, large dynamic ranges, label-free operation compatibility, and mechanical stability to name a few [30, 31]. Importantly, SIPH devices are inexpensive to fabricate and are highly reproducible [30] thanks to usage of CMOS fabrication principles. These devices have the ability to detect the influence of binding events on the optical evanescent field (the portion of guided wave electric field that travels on the outside of a waveguide) and are sensitive to small changes in refractive index [32]. Figure 2.2a depicts how the evanescent field has the ability to interact with bioreceptors along the outer border of the waveguide core. With the evanescent field's sensitivity to changes in refractive index due to binding events, an optical phase shift is induced [1, 31, 32]. In the case of MRRs, this appears in the form of a resonance wavelength shift, depicted by Figure 2.2b. The amount of shift that occurs is directly correlated to the change in the effective mode index, n_{eff} - the larger the change in n_{eff}, the larger the observed shift will be. Therefore, the resonance shift is also proportional to the

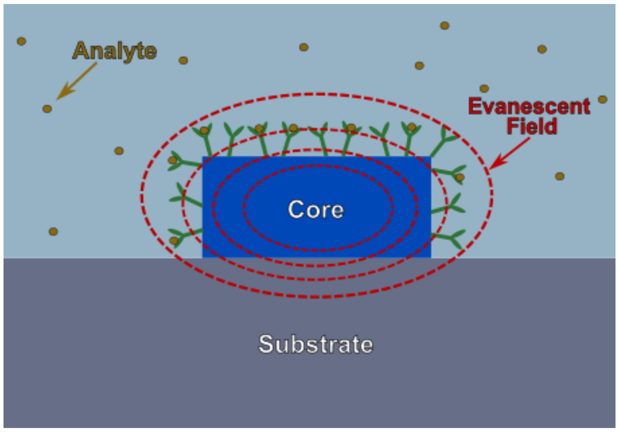

(a)

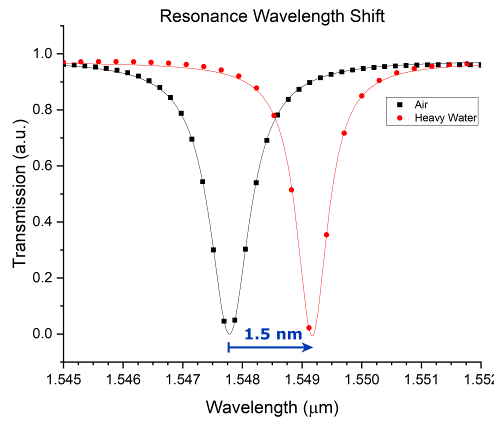

(b)

Figure 2.2: The evanescent field effect and induced resonance wavelength shift. (a) Diagram showing how an evanescent field can interact with bioreceptors. (b) Example of a resonance wavelength shift from a change in the upper cladding RI.

concentration of bound target analyte [1, 30, 32]. Typically, the spectrum is measured using a tunable laser alongside a photodetector or spectrum analyzer [30].

Some of the common configurations of SIPH devices used as biosensors that are able to detect concentrations down the the pg/mL consist of interferometers, Bragg gratings, and MRRs [30, 33–37].

Interferometers most commonly come in the form of Mach-Zender interferometers (MZI) and Young interferometers (YI). MZIs function by observing the interference in the output spectrum due to the phase shift caused by analyte binding in the sample arm. Since the interferometric-based readout can be complex, there has not yet been a successful commercial application of an MZI-based biosensor [38]. On the other hand, the YI does not recombine the two arms, and instead functions by comparing a phase shift induced by analyte binding in the sensing arm to the reference arm [32]. Increasing the length of the interferometer arms increases the sensitivity; however, false-positive signals are more likely to occur due to input source fluctuations and temperature variations [32, 38].

Bragg gratings are another type of commonly studied biosensor thanks to the strong evanescent field that is present in the gaps between sections of the waveguide core. When used as a biosensor, a phase-shifted cavity, in the form of a longer grating section, is typically formed in the middle of the gratings. In the optical readout, a resonance peak will appear in the stop-band, and this is used to observe RI changes [32].

2.5.1 Micro-Ring Resonators

An increasingly popular configuration for SIPH biosensors is the use of MRRs. These devices consist of a straight bus waveguide placed next to a ring of radius R. When light passes through the bus waveguide, given a suitable coupling gap and length, the light will couple from the bus into the ring.

Unlike the interferometric biosensors, MRR sensors are characterized mainly by the quality factor (QF). The QF is a measure of the ratio of energy stored inside the resonator to the energy dissipated per cycle - in this case, the amount of time it takes for the energy to decay to 1/e of it's original amount [32]. In literature, QF values for MRRs vary significantly, because a MRR's QF is heavily dependent on the mode polarization, radius, and waveguide core dimensions. When using the TM mode, the upper cladding medium also has a significant effect on the QF, because the TM mode is less confined in the waveguide. If the upper cladding is a lossy material at the functional wavelength (ie. H_2O at 1.55 μm), the QF suffers since circulating power from the mode is lost to the medium [32, 39].

An important aspect in designing ring resonators is optimizing the performance. The metrics for this are mainly based on quality factor and sensitivity of the device. A study by Schmidt et al. focuses on the optimization of a variety of different photonic devices for biosensing. In this paper they discuss the different possible ways in which ring resonators can be optimized. A summary of these are listed in Table 2.1, which is adapted from Schmidt et al [40]. The thin waveguides used in the TE mode enhance the evanescent field by having the mode be less confined, but this in turn decreases the QF and is not as compatible with current fabrication processes.

2.6 SIPH Modeling Techniques

As previously discussed in the introduction, the complex electromagnetic environment that encompasses MRRs can quickly turn modeling these devices into a challenge. A common approach that has been used in the past is the use of 2D simulations. These can be split into two main categories: cross-sectional simulations focused on mode analysis and top-down simulations of an entire system. Although they are very accurate and reliable, cross-sectional

	Configuration	Advantages	Tradeoffs
Increase Sensitivity	TE Mode, Thin Waveguide	Enhanced evanescent field	Not as compatible with current foundry processes
	TM Mode	Enhanced evanescent field	Increased losses due to higher radiation loss
	Slot Waveguide	Increased mode overlap with analyte in slot region	High loss
Increase QF	SiN waveguide	Higher quality factors thanks to less water losses	Requires the use of 850 nm wavelength which is not as common; SiN is more expensive
	1.3 μm Wavelength	Higher quality factors because of lower water absorption	Lower sensitivity from less evanescent field

Table 2.1: Advantages and tradeoffs of various MRR configurations based on increasing sensitivity or QF.

simulations can only be used to determine mode profiles. A study by Bahadori et al. contains a good example of using a cross sectional simulation to model mode profiles in various regions of a MRR system [4]. Using this model, they are able to estimate coupling coefficients in relation to different ring radii and coupling gaps.

On the other hand, 2D top-down simulations are a computationally efficient way of modeling a system; however, they encounter severe limitations in the reliability of the results. Because the model is 2D, the thickness of various elements cannot be defined and every element exists on the same plane - there exists no vertical layer differentiation in the model. Due to this, no upper and lower cladding material can be defined, and the thickness of the layer is approximated as an infinite slab. Calculating the propagated mode in this fashion causes the result to be far from the expected mode obtained from a cross-sectional simulation.

The most common methods of simulation in this domain are the Finite Difference Time Domain (FDTD) and the Finite Element Method (FEM). FDTD is a very common method for solving electromagnetic problems with a time-dependence. On the other hand, FEM works in steady-state, or in the frequency domain [5]. With both FDTD and FEM, distinct TE and TM modes of the waveguide core with accurate effective mode index (n_{eff}) values can be studied. These modes can then be propagated throughout a structure with great accuracy. A big advantage to 3D FEM is the flexibility of use with other physics problems such as heat transfer, fluid dynamics, and surface chemistry to simulate much more robust models.

The most common simulation method in literature is FDTD, and a few good examples of these include [41–44]. For applications such as biosensing; however, the FDTD method encounters some limitations. The study by Ali et al. demonstrates this by having the model approximate various analytes as as aqueous medium based on the refractive index (RI) of blood [43]. Although this works and resonance shifts can be observed, it ignores the effect that analyte concentration has on the overall RI of the medium. Another study by Fard et al. encounters the same issue, but works around it by measuring sensitivity based on glucose concentration in water which does not require any binding events [44].

2.6.1 The Finite Element Method

The Finite Element Method (FEM) is a way of solving complex engineering problems numerically. This process involves the conversion of partial differential equations (PDE) into sets of linear algebraic equations to approximate the solutions of boundary-value problems [45]. With these models it is possible to accurately assess designs to make the design process more cost effective and safer [46].

The basis of FEM lies in the aspect of meshing. A model used in a FEM simulation consists of thousands to millions of small interconnected geometric parts which together form a mesh that encompasses the entire geometry. These elements do not overlap, but instead fill the volume of the model [46]. The main way to increase the accuracy of a FEM model is to decrease the size of meshing elements [46]. However, this comes with the drawback of requiring much more processing power as the mesh is made finer. FEM works by applying physics equations to nodes of the interpolated mesh elements that comprise the entire morel geometry. Typically the preferred mesh elements are linear and non-curved. In 2D models four-node quadrilateral elements are typically used, whereas in 3D models eight-node bricks are preferred [46]. The meshing process is a significant challenge for humans, so computer-aided processes have been developed to automize the mesh generation for any given geometry [46]. Users can specify the desired mesh type and maximum and minimum element sizes in specific regions, but overall, little control over the resulting mesh is available. Automatic mesh generation procedures are split into two main categories: mapped meshes and free-form meshes. Mapped meshes typically are only applied to basic, regular structural models as well as some fluid domains.

To improve FEM model accuracy while keeping the computational complexity relatively low, graded meshes are used. A graded mesh contains portions of high-quality mesh elements in the main regions of interest of the model.

Chapter 3

Theory

3.1 Evanescent Fields

When total internal reflection (TIR) occurs inside a waveguide, rays of light reflect off the edges of the waveguide, generating an exponentially decaying field into the surrounding medium along the outer edges. Figure 3.1, adapted from McGarvey [47], depicts this interaction. This field is known as the evanescent field, and it is the main mechanism that contributes to coupling between waveguides [47]. The evanescent field also has a significant effect on sensing, because it makes the traveling mode more susceptible to changes in RI due to binding events.

In a basic optical waveguide system, light travels in the form of modes that are most commonly confined to the core of the waveguide. The evanescent field of the mode is the

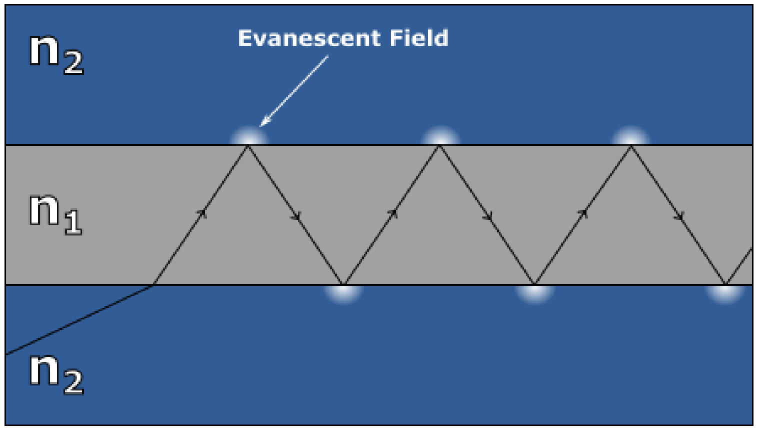

Figure 3.1: Example of how an evanescent field is generated as a result of light reflecting off the edges of a waveguide.

portion that extends outside of the waveguide core. Figure 2.2a, shows generally how the field extends into the surrounding medium. The further away from the center of the core, the weaker the field becomes. This portion of the mode is much more sensitive to RI changes in the medium and imperfections of the structure. Typically, the evanescent field portion of the TE mode is significantly less prominent than that of the TM mode. Figure 3.2 shows the mode profile of the TE and a TM mode of the same waveguide, and the difference in prominence of the evanescent field can clearly be observed.

The evanescent field in the surrounding medium of a waveguide decays at an exponential rate as it gets further from the edge of the waveguide. The penetration depth, d_e, is defined using equation 3.1, where n_{eff} is the effective index, n_{clad} is the RI of the cladding, and λ_{res} is the operating wavelength [40]. The penetration depth represents the distance where the field decays to 1/e of it's original value [48].

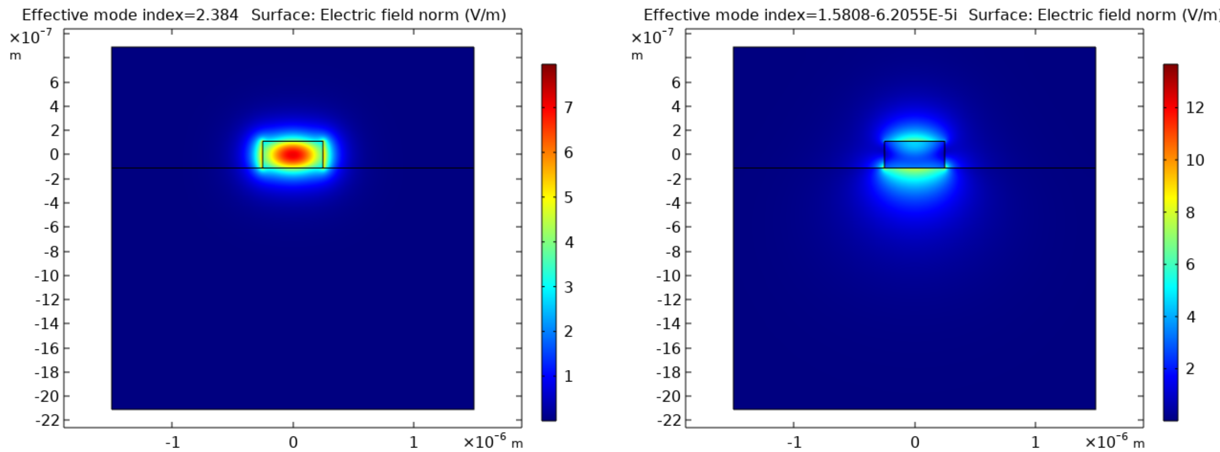

Figure 3.2: The TE (left) and TM (right) mode profile of a 500 nm x 220 nm waveguide with an air upper cladding.

$$d_e = \frac{\lambda_{res}}{2\pi\sqrt{n_{eff}^2 - n_{clad}^2}} \tag{3.1}$$

3.2 Optical Ring Resonators

Photonic micro-ring resonators are small structures typically composed of a ring and bus waveguides made from Silicon. The cross-sections of these waveguide cores are most commonly rectangular. The core tends to be placed on top of an oxide substrate layer and covered by a medium such as air. Various applications such as biosensing may require the upper cladding medium to be water or some other liquid. Silicon is most commonly chosen as the core thanks to its high RI being 3.4757 at a wavelength of 1.55 μm [49]. The large difference between the RI of the core and cladding materials allows for light to achieve TIR inside the waveguide, resulting in a guided mode as depicted in Figure 3.1.

Figure 3.3a and 3.3b depict the general configurations for all-pass and add-drop ring resonators. An analytical model for both configurations can be defined using slightly different sets of equations. The matrix relation seen in equation 3.2 can be used to describe the mode amplitudes, E, at different points along the structure [50].

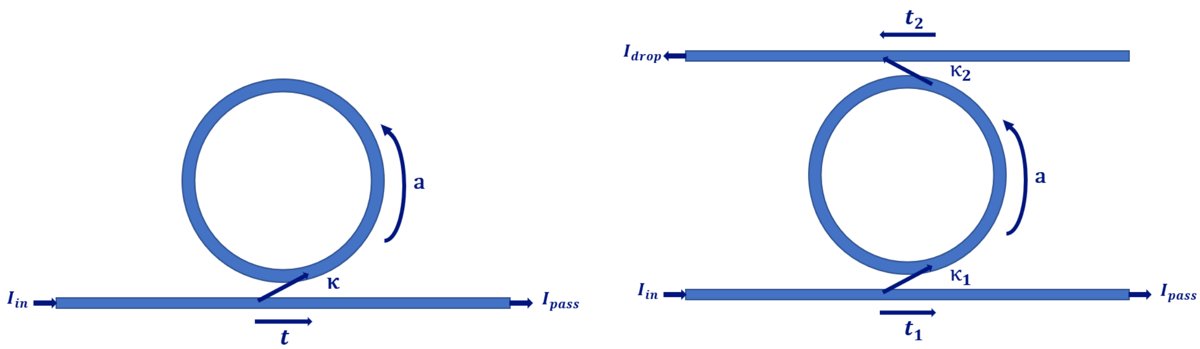

(a) Schematic of a single-bus ring resonator. **(b)** Schematic of an add-drop ring resonator.

Figure 3.3

$$\begin{bmatrix} E_{t1} \\ E_{t2} \end{bmatrix} = \begin{bmatrix} t & \kappa \\ -\kappa^* & t^* \end{bmatrix} \begin{bmatrix} E_{i1} \\ E_{i2} \end{bmatrix} \tag{3.2}$$

Next, the E_{i1}, E_{i2}, E_{t1}, and E_{t2} terms need to be defined according to their positions along the structure. E_{i1}, the input amplitude is set to equal 1 for simplicity. Equations 3.5a through 3.5c define the modal amplitudes at the other positions. E_{i2} is the amplitude in the ring after one round-trip, E_{t1} is the amplitude at the output port, and E_{t2} is the amplitude in the ring immediately after light couples from the bus waveguide. From this matrix and definitions of the variables contained, equations for an analytical model can be described.

$$E_{i1} = 1 \tag{3.3a}$$

$$E_{i2} = a \cdot e^{j\theta} E_{t2} \tag{3.3b}$$

The single-pass transmission coefficient of the ring, a, accounts for both the propagation loss in the ring and the loss from the couplers [39]. A lossless system will have a value of a equal to one. The a value also relates to the power attenuation coefficient, α, through equation 3.4a, where L is the round-trip length. The propagation constant, β is defined in equation 3.4b as a function of the effective refractive index and wavelength. Then θ, the single-pass phase shift, can be defined by multiplying β with L ($2\pi r$).

$$a^2 = e^{-\alpha L} \tag{3.4a}$$

$$\beta = k \cdot n_{eff} = \frac{2\pi n_{eff}}{\lambda} \tag{3.4b}$$

$$\theta = \beta \cdot 2\pi r = \frac{4\pi^2 r n_{eff}}{\lambda} \tag{3.4c}$$

The rest of the modal amplitudes can then be defined using the variables E_{t1}, E_{i2}, and E_{t2}. These can be seen in equation set 3.5.

$$E_{t1} = \frac{-a + t \cdot e^{-j\theta}}{-at^* + e^{-j\theta}} \tag{3.5a}$$

$$E_{i2} = \frac{-a\kappa^*}{-at^* + e^{-j\theta}} \tag{3.5b}$$

$$E_{t2} = \frac{-\kappa^*}{1 - at^* e^{j\theta}} \tag{3.5c}$$

The coupling and loss coefficients of a single-bus ring resonator can be extracted by using the equation 3.6 from Bogaerts et al [39].

$$T_n = \frac{I_{pass}}{I_{input}} = \frac{a^2 - 2tacos(\phi) + t^2}{1 - 2atcos(\phi) + (ta)^2}, \quad \phi = 0, \pi \tag{3.6}$$

Since this equation has two unknowns, a and t, equation 3.6 must be solved for both on and off resonance. Therefore two equations can be derived from equation 3.6, where off-resonance uses the condition $\phi = \pi$, and on-resonance uses the condition $\phi = 0$. By substituting transmittance values for T_{on} and T_{off}, the values for t and a can be solved for.

$$T_{on} = \frac{I_{pass}}{I_{in}} = \frac{a^2 + 2ta + t^2}{1 + 2at + (ta)^2} \tag{3.7a}$$

$$T_{off} = \frac{I_{pass}}{I_{in}} = \frac{a^2 - 2ta + t^2}{1 - 2at + (ta)^2} \tag{3.7b}$$

Since this is a system of polynomial equations, a root finding algorithm is used to find all possible solutions. Then, all values that are imaginary and/or greater than 1 or less than zero are filtered out. A study by McKinnon et al. points out that the resulting values can be interchanged in equation 3.6, yielding identical results if the values are swapped [51].

The solutions can be disentangled by plotting the coefficients in relation to the wavelength, because the loss coefficient, a, stays relatively constant as wavelength changes [51].

In an ideal ring resonator in which no coupling losses occur, equation 3.8 holds, where κ is the cross-coupling coefficient.

$$t^2 + \kappa^2 = 1 \tag{3.8}$$

After extracting the self-coupling coefficient, t, and the round-trip loss coefficient, a, the expected transmission curve of the APMR can be plotted using equation 3.9.

$$P_t = |E_t^2| = |(\frac{-a + te^{-j\theta}}{-at^* + e^{-j\theta}})^2| \tag{3.9}$$

In a double-bus or add-drop configuration, the set of equations changes, but remain similar. Equations 3.10a and 3.10b are used to derive the equations for transmittance on and off resonance at both the through-port ($\mathrm{T_p}$) and drop-port ($\mathrm{T_d}$) [39].

$$T_p = \frac{I_{pass}}{I_{input}} = \frac{t_2^2 a^2 - 2t_1 t_2 acos(\phi) + t_1^2}{1 - 2t_1 t_2 acos(\phi) + t_1 t_2 a}, \quad \phi = 0, \pi \tag{3.10a}$$

$$T_d = \frac{I_{drop}}{I_{input}} = \frac{(1 - t_1^2)(1 - t_2^2)a}{1 - 2t_1 t_2 acos(\phi) + t_1 t_2 a}, \quad \phi = 0, \pi \tag{3.10b}$$

Substituting in the values for ϕ, equations 3.11a through 3.11d are obtained. Where $T_{t|on}$ is transmittance at the through-port on resonance, $T_{t|off}$ is the through-port transmittance off resonance, $T_{d|on}$ is the drop-port transmittance on resonance, and $T_{d|off}$ is the drop-port transmittance off resonance. These equations appear as R_{min}, T_t, T_{max}, and T_d, respectively in the paper by Bogaerts et al [39].

$$T_{t|on} = \frac{(t_2 a - t_1)^2}{(1 - t_1 t_2 a)^2} \tag{3.11a}$$

$$T_{t|off} = \frac{(t_2 a + t_1)^2}{(1 + t_1 t_2 a)^2} \tag{3.11b}$$

$$T_{d|on} = \frac{(1 - t_2^2)(1 - t_2^2)a}{(1 - t_1 t_2 a)^2} \tag{3.11c}$$

$$T_{d|off} = \frac{(1 - t_2^2)(1 - t_2^2)a}{(1 + t_1 t_2 a)^2} \tag{3.11d}$$

Equations 3.11a through 3.11d can be used to form new equations based on the power ratios in the through-port and drop-port for both on and off resonance. These power ratios can be visualized in the transmittance curve from Figure 3.4. The coupling coefficients, t_1, t_2, and a can then be extracted by using the system system of equations formed by 3.12a, 3.12b, and 3.12c. Finally, κ can be computed using the relationship $\kappa_n = \sqrt{1 - t_n^2}$. The entanglement of coefficients investigated by McKinnon et al. [51] also applies to ADMR configurations; however, it may be more difficult to disentangle t_1 and t_2 from each other. This process involves plotting the a, t_1, and t_2 coefficients along a varying wavelength to compare the shapes of the curves. McKinnon et al. suggests that for an APMR, the curve for a stays relatively constant, whereas the value of t decreases as the wavelength increases [51]. For an ADMR, introducing an additional unknown in the form of t_2 could lead to confusion when comparing t_1 and t_2 against a varying wavelength, because they will likely have similar curves.

$$ER_{on} = \frac{T_{t|on}}{T_{d|on}} \tag{3.12a}$$

$$ER_{off} = \frac{T_{t|off}}{T_{d|off}} \tag{3.12b}$$

$$ER_{d} = \frac{T_{d|on}}{T_{d|off}} \tag{3.12c}$$

Using the extracted parameters of t_1, t_2, κ_1, κ_2, and a, the expected transmittance curve of the add-drop ring resonator can be plotted using equations 3.13a and 3.13b [50]. The output power, P_{t1} and P_{t2}, is obtained by taking the square of the absolute value of E_{t1} and E_{t2}. This can then be plotted against either wavelength or frequency on the x-axis.

$$E_{t1} = \frac{t_1 - t_2^* a e^{j\theta}}{1 - t_1^* t_2^* a e^{j\theta}} \tag{3.13a}$$

$$E_{t2} = \frac{-\kappa_1^* \kappa_2 a_{1/2} e^{j\theta_{1/2}}}{1 - t_1^* t_2^* a e^{j\theta}} \tag{3.13b}$$

3.2.1 Quality Factor

As previously discussed, when measuring or simulating a MRR, the QF is one of the most important parameters to track. The QF is inversely related to the total loss experienced by the system. These sources include but are not limited to coupling and radiation losses [52].

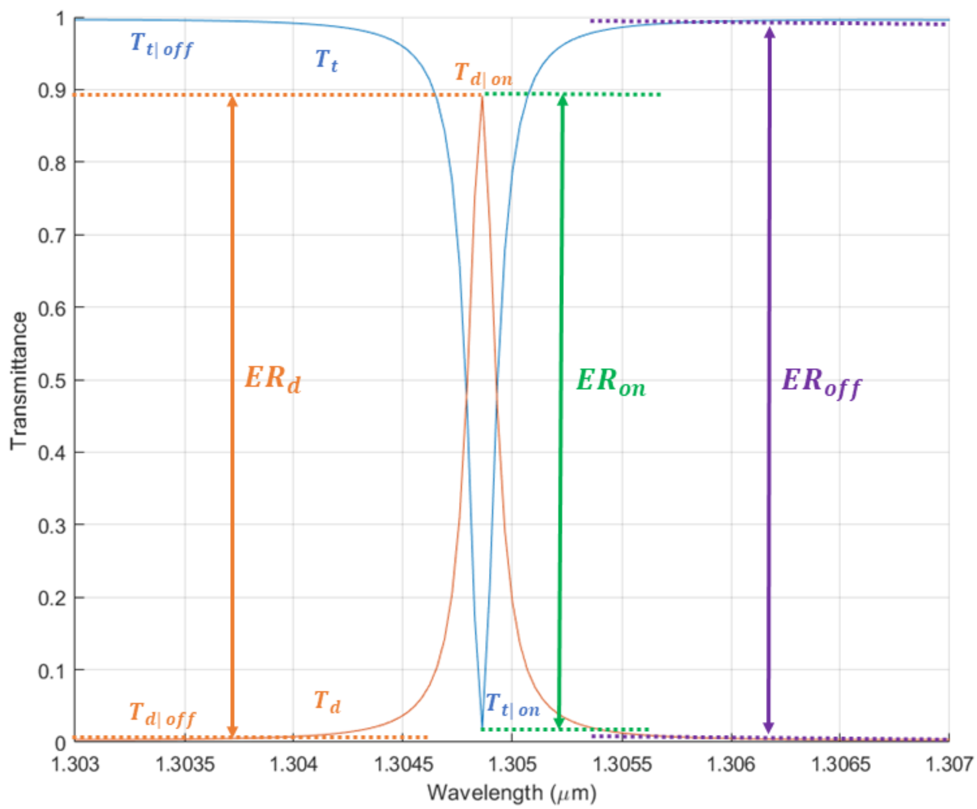

Figure 3.4: Transmission spectrum of an add-drop ring resonator, where blue is the through-port and orange is the drop-port. Information used for extracting coupling coefficients is included. For this particular system, $a = 0.99508, t_1 = 0.93224, t_2 = 0.95229$.

The QF is most commonly defined as the ratio of stored energy inside the resonator to the energy dissipated per cycle. In equation 3.14, W is the stored power, ω_0 is the angular frequency, and P_{loss} represents all the loss mechanisms [52]. Mutiple QFs contribute to the P_{loss} term, most notably the intrinsic QF, Q_i, and the coupling QF, Q_c. Shown in equation 3.15, the total or loaded QF, Q_t, is defined as the reciprocal sum of the intrinsic and coupling QFs.

$$Q = \omega_0 \frac{W}{P_{loss}} \tag{3.14}$$

$$\frac{1}{Q_t} = \frac{1}{Q_i} + \frac{1}{Q_c}; \quad P_{loss} = P_i + P_c \tag{3.15}$$

The intrinsic QF describes the QF of an isolated ring resonator. This value is always magnitudes larger than the total QF, because there are no losses due to coupling. These losses tend to be the dominant term in equation 3.15.

When calculating QF values from results, only the total QF, Q_t is considered. Rather than using equation 3.14 to calculate it, equations 3.16a and 3.16b below are used, depending on if the MRR is in the all-pass or add-drop configuration [39]. Another way to calculate the QF without needing the t and a coefficients is to divide the resonant frequency by the FWHM of the resonance peak, shown in equation 3.16c [53].

$$Q_{APMR} = \frac{\pi n_g L \sqrt{ta}}{\lambda_{res}(1 - ta)} \tag{3.16a}$$

$$Q_{ADMR} = \frac{\pi n_g L \sqrt{t_1 t_2 a}}{\lambda_{res}(1 - t_1 t_2 a)} \tag{3.16b}$$

$$Q = \frac{\lambda_{res}}{FWHM} \tag{3.16c}$$

3.2.2 Performance Optimization

Ring resonators are usually designed such that they reach the critical coupling condition for maximum performance. Critical coupling in an APMR occurs when $t = a$ and the transmission in the through-port on resonance goes to zero. Over-coupling occurs when the ring is too close to the bus waveguides, and under-coupling occurs when the ring is too far from the bus waveguides. Figure 3.5 shows the slight difference between transmission in an over-coupled, under-coupled, and critically-coupled APMR. To discern the coupling regime of the system, a couple methods can be used.

First, the self-coupling coefficient and the single-pass amplitude coefficient can be compared. A relationship between these coefficients exists, defined by the set of inequalities in equation 3.17, which determines the coupling regime of the system in an APMR configuration. When $t < a$ the system is overcoupled, when $t > a$ the system is undercoupled, and when $t = a$ the system is critically coupled [54, 55].

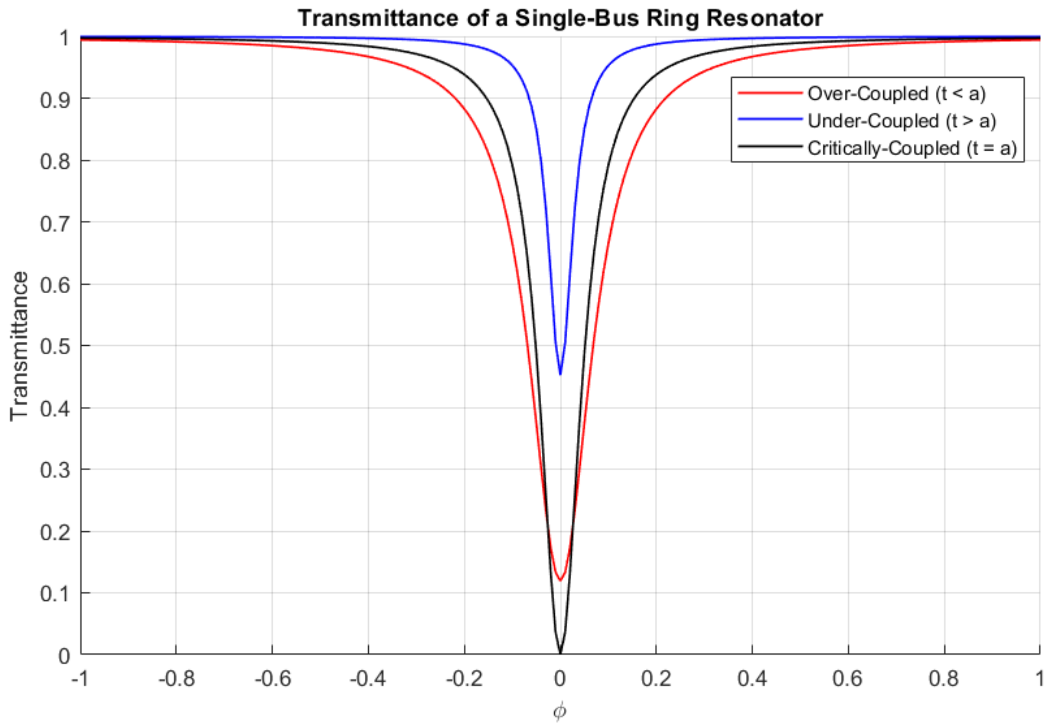

Figure 3.5: The difference in transmittance for a single-bus ring resonator in the three coupling regimes. The value for a is set to be constant at $a = \sqrt{0.95}$.

$$t < a, \quad t > a, \quad t = a \tag{3.17}$$

To show the difference between the three coupling regimes in an APMR, equation 3.9 can be used to plot the transmission curve using differing values of a and t. Figure 3.5 shows the difference in transmission in the three coupling regimes for an APMR. For over-coupling $t = \sqrt{0.9}$, and for under-coupling $t = \sqrt{0.99}$.

Another way to characterize the coupling regime is by observing the resonance depth as the coupling gap changes [54]. The resonant depth is defined as the height of the resonance peak in arbitrary units (from 0 to 1), using the normalized transmission. This can also be defined using equation 3.18 [54]. Note that this equation only holds for a single-bus configuration. Plotting this equation with a constant value of a and a varying t, the relationship defined in equation 3.17 becomes clear. Figure 3.6 shows how κ_1 and the resonance depth, h, change as a function of t_1 when a is set to a constant value of 0.95.

$$h = 1 - (\frac{t-a}{1-ta})^2 \tag{3.18}$$

In an add-drop configuration, the same process can be used, but by replacing equation 3.6 with equations 3.10a and 3.10b. Due to the relationship of $t_2 a = t_1$ defining critical coupling for an add-drop resonator, the coupling regimes must be changed slightly. Figure 3.7 shows the difference in transmission between the different coupling regimes in an add-drop configuration.

It is clear that in an over-coupled resonator the width of the resonance peak is wider than that of a critically-coupled one, and in an under-coupled resonator the peak is narrower. The resonance depth directly relates to the sensitivity of the resonator through the SNR [56]. As the resonance peak width (FWHM) decreases, the QF of the resonator increases; however, a lower SNR will be achieved due to having a much smaller resonance depth [54].

The other important parameters to optimize for biosensing applications are the bulk sensitivity, surface sensitivity, and limit of detection (LoD). Bulk sensitivity is defined as the

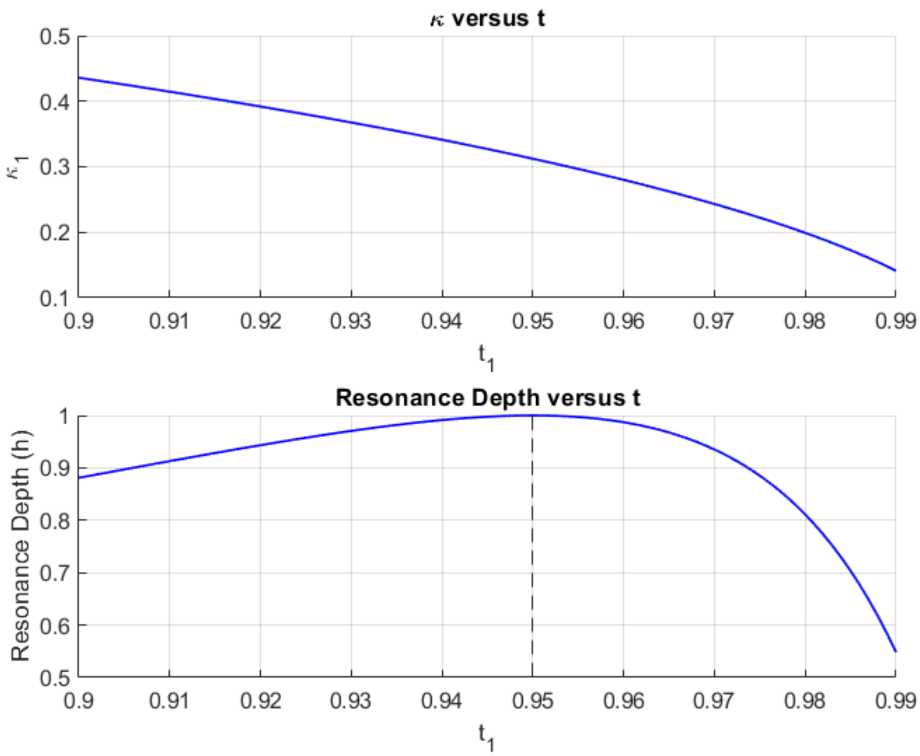

Figure 3.6: Plot showing the relationship between κ and t (above) and the relationship between resonance depth (h) and t (below). Critical coupling occurs on the dashed line ($h = 1$, $t = 0.95$). The value of a is a constant 0.95.

change in resonance wavelength versus the change in refractive index of the fluid cladding, whereas surface sensitivity is defined as the change in resonance wavelength versus the change in thickness of the homogeneous adlayer. Using these equations, the LoD for a resonant cavity sensor, defined as the minimum detectable change in RI or mass, can be described with equation 3.19c [32, 53, 57]. To maximize the bulk sensitivity, $\mathrm{S_{bulk}}$, the largest possible change in resonant wavelength, $\Delta\lambda$ must be achieved over a small change in cladding RI (Δn_{fluid}). Typically, this is done by using the TM mode thanks to the presence of a large evanescent field [32, 58, 59].

$$S_{bulk} = \frac{\Delta\lambda}{\Delta n_{fluid}} \tag{3.19a}$$

$$S_{surf} = \frac{\Delta\lambda}{\Delta t_{adlayer}} \tag{3.19b}$$

$$LoD = \frac{\lambda}{QS}, \quad S = S_{surface} \quad or \quad S_{bulk} \tag{3.19c}$$

Another advantage of the TM mode is that it experiences significantly less scattering losses due to sidewall roughness, because the evanescent field is much more concentrated above and beneath the waveguide [32, 40]. Lee et al. investigated the effect of sidewall roughness on the transmission loss of various waveguides in the TE mode, and they found that for a waveguide width of 500 nm, the transmission loss is approximately 35-40 dB/cm for a roughness root-mean-square value (σ) of 10 nm [60]. Similarly, a study by Qiu et al. optimizes the propagation losses by reducing the sidewall roughness from fabrication. This results in a σ of 2.75 nm and a propagation losses of approximately 2.5 dB/cm and 0.5 dB/cm for the TE and TM mode, respectively [61].

The effects of waveguide structure tolerances on various parameters such as QF, n_{eff}, and the self-coupling coefficient has been investigated. Prinzen et al. show that variations in Δ_{Clean}, the tolerance on waveguide cross-section due to silicon etching, have significant impact on the resulting QF and n_{eff} of ring resonators [62]. A Δ_{Clean} of 5 nm can result in the QF of a MRR decreasing by approximately 8.7% and the n_{eff} decreasing by approximately 2% [62]. Another study by Grosman et al. suggests that variations in sensitivity of a MRR used for biosensing arose from lithography fabrication tolerances [63]. In this study, the measured sensitivity varied by approximately 10 nm/RIU for MRRs with a 200 μm radius [63].

3.3 MRR Modeling Using FEM

Due to the mathematical complexity of the MRR structure, the partial differential equations (PDEs) that define light propagation throughout the structure are not solvable analytically. Therefore, some approximations must be made - typically by discretization. The FEM preforms this by using numerical model equations and applying them to a mesh to approximate the PDEs [64].

In general, if u is a dependent variable in a PDE, it can be approximated using a function of linear combinations, u_h. Equations 3.20a and 3.20b show the most basic form of this relationship, where ψ_i represents a basis function, also known as an interpolation function

[45, 46, 64, 65]. This equation interpolates the element geometry for q nodal points in all coordinate directions, x, y, and z, which are represented by u_i.

$$u \approx u_h \tag{3.20a}$$

$$u_h = \sum_{i}^{q} u_i \psi_i \tag{3.20b}$$

When using FEM to simulate a waveguide system in 3D, the electric field of the traveling wave is defined as Equation 3.21. In this equation, E_1 represents the slowly varying field envelope and ϕ is the approximation of the propagation phase.

$$E = E_1 e^{-j\phi} \tag{3.21}$$

The outer boundaries of the 3D model are defined using a scattering boundary condition (SBC), which makes selected boundaries appear transparent to incoming and scattered plane waves. This significantly reduces any unwanted reflections that would cause noise in the surrounding media. Equation 3.22 defines the electric field at the SBC boundary, where E_0 is the incident plane wave traveling in direction k [66], n is the normal vector to the boundary, E_{sc} is the electric field of the scattered wave, and r is the position vector.

$$E = E_{sc} e^{-jk(n \cdot r)} + E_0 e^{-jk(k \cdot r)} \tag{3.22}$$

The input port of the model injects a mode into the structure, and the output ports absorb these modes. Analysis of these modes at the port boundaries is known as boundary mode analysis (BMA). The electric field at the input and output ports is defined in equation 3.23. In this equation, E is the electric field on the port boundary, r is the position vector, E_{inc} denotes the incident electric field, S_i is the S-parameter, E_i is the mode field, α_i is the mode's propagation constant, n is the normal vector, and r_0 is the position on the port boundary [66].

$$E(r) = E_{inc}(r) + \sum_i S_i E_i(r) e^{-\alpha_i n(r-r_0)} \tag{3.23}$$

Practically speaking, any structure has an infinite amount of degrees of freedom (DOF). Thus for FEM, a mesh is constructed for the geometry to limit the number of DOF to make computations possible. In 3D, the mesh elements come in a variety of shapes, most notably tetrahedra, hexahedra, triangular prisms, and pyramids. A generated mesh comprises the entirety of the model, and equations can be applied to each element in the mesh. In this case the propagated wave equation, 3.23, is applied to each mesh element as indicated by the position along the port boundary, r_0, and the position vector, r.

In addition the use of eigenfrequency analysis is used to calculate the intrinsic QF, $\mathrm{Q_i}$ of the MRR. Equation 3.24 defines the electric field as a function of the position vector, r, and time, t. The eigenvalue takes the form of $(-\lambda) = -\delta + j\omega$, where the imaginary part represents the eigenfrequency, and the real part represents damping in time. More commonly, equation 3.25 is used to define the QF, derived from the eigenfrequency, ω, and the damping, δ, also known as the ring-down time.

$$E(r,t) = Re(\tilde{E}(r_T)e^{j\omega t}) = Re(\tilde{E}(r)e^{-\lambda t}) \tag{3.24}$$

$$Q = \frac{\omega}{2|\delta|} \tag{3.25}$$

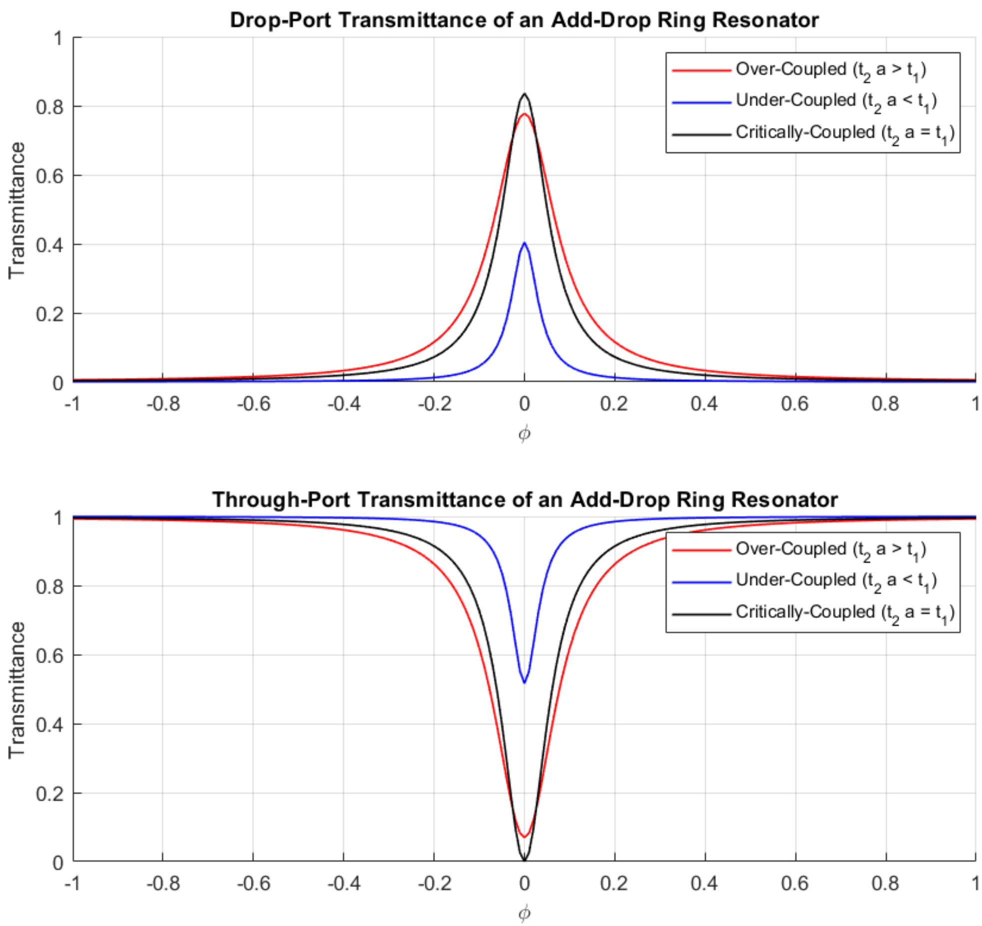

Figure 3.7: Transmittance of an add-drop ring resonator for over, under, and critical coupling. For these plots, $t_2 = \sqrt{0.95}$ and $a = \sqrt{0.99}$. For over-coupling $t_1 = \sqrt{0.9}$, for under-coupling $t_1 = \sqrt{0.99}$, and for critical-coupling $t_1 = t_2 a$.

Chapter 4

FEM Implementation

4.1 Three-Dimensional FEM Simulations

COMSOL Multiphysics version 6.0 (Electromagnetic Waves, Beam Envelopes (EWBE) module) is used to simulate three-dimensional models of the ring resonators. Comsol simulates the model by using the finite element method (FEM), taking the specified mode from preliminary boundary mode analysis (BMA) and propagating it throughout the structure. For this simulation to work, the direction of propagation needs to be defined by equations using the propagation constant, β, and structure of the ring. The model is split up into three regions: the through-port waveguide and a portion of the ring where coupling occurs, the ring where no coupling occurs, and the drop-port waveguide where coupling occurs again. These sections can be visualized in Figures 4.1 and 4.2.

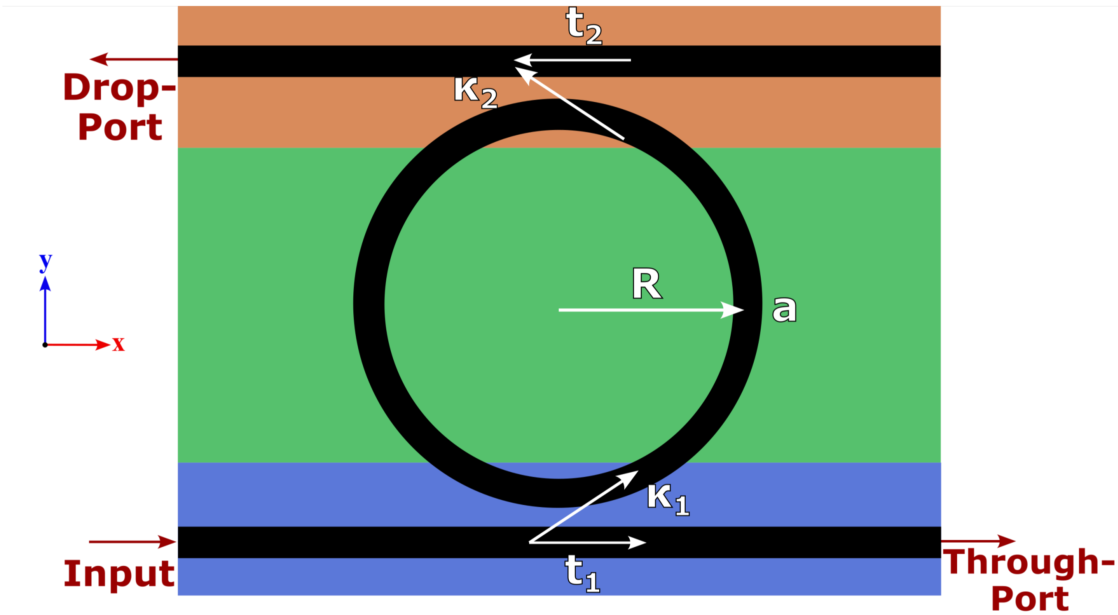

Figure 4.1: Top-down view of the color-coded sections of the ring resonator model defining direction of propagation. Blue is the through-port section, green is the ring section, and orange is the drop-port section.

The phase, ϕ, in each region of the model is defined using the set of equations 4.1 and defines the propagation direction of the mode throughout the model. In these equations, β is the propagation constant, R is the radius of the ring, and x and y represent the direction of propagation.

$$\phi = \begin{cases} \beta x & \text{Input waveguide} \\ \beta R \arctan\left(\frac{-x}{y}\right) & \text{Ring} \\ \beta(-x) & \text{Output waveguide} \end{cases} \tag{4.1}$$

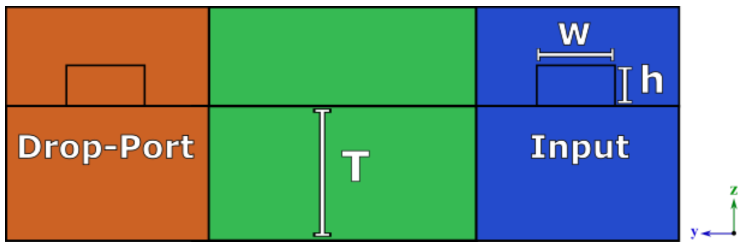

Figure 4.2: Cross-sectional view of the color-coded sections at the input and drop-port side of the ADMR.

The material definition of the waveguide can be customized for the ability to account for sidewall roughness, which by default is not accounted for. This can be done by converting measured loss values (dB/cm) into the extinction coefficient of the material. Equation 4.2a is used to convert loss in units of dB/cm to units of 1/m. Equation 4.2b [67] uses this converted value of α to calculate the extinction coefficient, k, to be used in the material definition.

$$\alpha \ \ [\frac{dB}{cm}] \cdot \frac{100 \ \ cm}{m} \cdot \frac{ln(10)}{10} = \alpha \ \ [\frac{1}{m}] \tag{4.2a}$$

$$\alpha[\frac{1}{m}] = \frac{4 \cdot \pi \cdot k}{\lambda_0} \tag{4.2b}$$

4.1.1 Boundary Conditions

For the model to work correctly, boundary conditions along the outer borders of the structure must be defined. Input and output ports are used to define the input and output regions of the system. A port with excitation turned on is defined at the input, and ports with excitation set to off are defined at the through and drop port regions. As mentioned previously, along the remaining outer boundaries of the model, the Scattering Boundary Condition (SBC) was chosen so that light would not reflect back into the model after hitting the edges. A field continuity condition is used on the inside of the model where the ring is divided to prevent any possible discontinuity. The divisions can be seen in Figure 4.1 between the orange and green sections and the blue and green sections.

4.1.2 Meshing

The mesh of the structure consists of several main parts - a mesh for the bus waveguides, a mesh for the ring, and a mesh for the top and bottom claddings. The different meshing styles are shown in Figures 4.3a and 4.3b. The bus waveguides are made up of a swept mesh with the cross-sectional faces being made up of triangular elements, and the transverse faces are made up of prismatic elements. The swept mesh is generated by expanding a face consisting of triangular elements over an array of specified length, turning them into triangular prisms. Having this blend makes the simulation much more efficient as opposed to having a triangular mesh making up the entire waveguides. On the other hand, the ring consists only of triangular elements. The ideal mesh for the ring would be swept, similarly to the bus waveguides; however, the division of the ring for the definitions section causes this to be unfeasible. Dividing the ring in this fashion creates faces that are not normal to the sidewalls of the ring, causing the mesh to become distorted as it approaches the division line. Finally, the cladding regions are made up of a coarse mesh using only triangular elements.

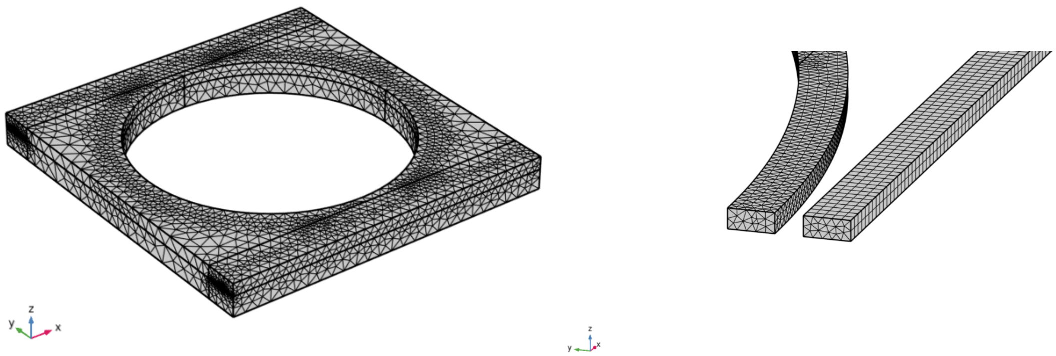

(a) Meshing of entire the ADMR model, showing the cladding mesh.

(b) Meshing of the bus waveguide (right) and the ring (left).

Figure 4.3: Figure showing the mesh of the entire model (a), and the difference in meshing of the waveguides (b). In (b), the bus waveguide (right) consists of a swept mesh, whereas the ring (left) consists of a free-tetrahedral mesh.

The quality of the mesh has a significant effect on the overall results of the simulation. In the mesh settings, the maximum element size is specified depending on the model's dimensions. The model can then be simulated with varying mesh quality, and results can be compared afterwards.

4.1.3 Preliminary Boundary Mode Analysis

Prior to performing a simulation of the entire structure, BMA steps are performed for each of the ports of interest: one for the input, through-port, and drop-port. COMSOL's BMA solver works by solving for effective mode indices around the specified refractive index (RI). In this scenario the waveguide core is Silicon, so the solver searches for modes around the RI

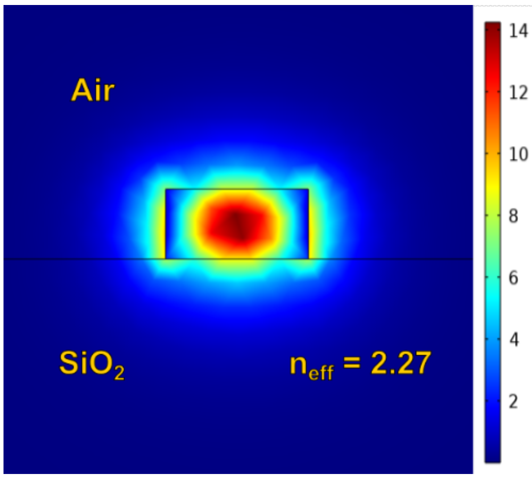

(a) Resulting BMA of the TE mode of the 450 nm x 220 nm waveguide core.

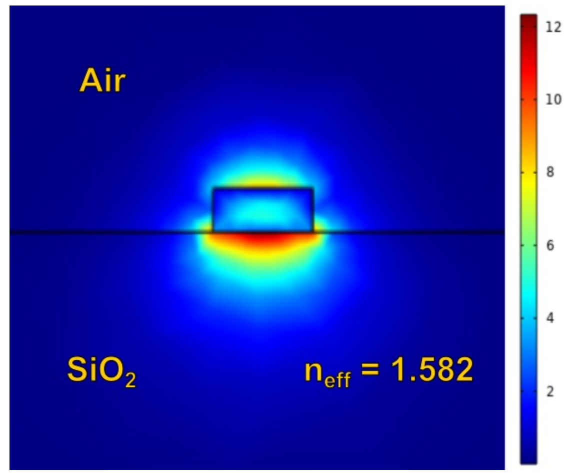

(b) Resulting BMA of the TM mode of the 500 nm x 220 nm waveguide core.

Figure 4.4: BMA results of the two different simulated configurations.

of Silicon (3.4757 at 1550 nm) [49]. The BMA solver computes the modes, and they must be analyzed to determine which one to propagate. The TE mode usually has the higher RI than the TM mode.

To discern between the TE and TM modes, the boundary mode profile is analyzed. Displaying this variable on the model's port surfaces shows the electric field profile depending on the effective mode index. For example, Figures 4.4a and 4.4b show the preliminary BMA plots for both the TE and TM mode. Both of these modes are taken at a wavelength of 1.55 μm with an Air cladding. Once the mode is chosen, the computed effective mode indices are inserted back into their corresponding BMA steps, and a parametric sweep of the wavelength is incorporated.

Chapter 5

Results and Discussion

5.1 FEM Simulation Results and Analysis

A large number of simulations on varying MRR parameters were run. For this system utilizing 16 GB of RAM and an Intel©Core^{TM} i7-10750H CPU, it was concluded that using a 15 μm radius was the largest feasible size for three-dimensional FEM simulations. Larger models caused significant performance issues, and not enough memory was available for the computations, causing simulations to crash.

An unexpected parameter that turned out to have a significant impact in the final results was the buried oxide (BOX) cladding thickness. In literature, the most commonly used SiO_2 thickness in these sensing devices is 2 μm [32,68]. The BOX thickness used in the fabrication of the rings is also 2 μm [69]. Originally, the models had a BOX thickness of 1 μm to decrease the computational complexity; however, this caused anomalies in the results when changing the top cladding medium. More specifically, using an air cladding caused a significant drop in quality factor and increase in propagation loss when compared to H_2O and D_2O. The presence of an air cladding forces more of the evanescent field of the TM mode into the BOX substrate, because of the larger difference in RI between air and silicon in comparison to Silicon and SiO_2. Since the outer bounds of the model use a SBC, any portion of the mode propagating near the bounds will get scattered out of the model, causing a large source of loss observed in the extinction coefficient. Figure 5.2 demonstrates the difference in mode profiles with various upper cladding media, and the mode being forced into the substrate when an air cladding is used can be observed. This phenomenon is confirmed in literature, where increasing the BOX thickness exponentially decreases the substrate leakage [70]. Using a 2 μm substrate thickness allows for the loss due to the leakage to be negligible for TE modes and on the order of 0.001 dB/cm for TM modes [39].

5.1.1 Comparison of Boundary Mode Analyses

Figures 5.1 and 5.2 show the results for the 2D cross-sectional simulations. A very slight difference in the mode profile can be noticed between Figure 5.1a and 5.1b, where there is a little more concentration on the sides of the waveguide. This is expected, because smaller waveguides are less capable of confining light [40]. In comparison to 2D, the quality of the BMA in the 3D model suffers as an effect of the reduced meshing quality; however, it is clear that the resulting modes are comparable, confirming the accuracy of the 3D model. The 3D model's TM modes at the 1.55 μm wavelength are depicted later in Figure 5.3.

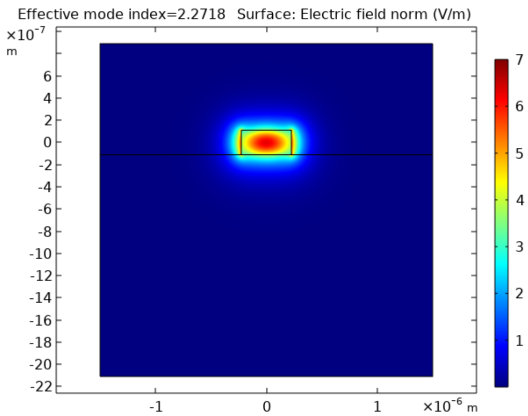

(a) 2D simulation of the cross-sectional TE mode profile of a 450 nm x 220 nm waveguide. The upper cladding is air and the substrate is SiO_2. The n_{eff} value is 2.2718.

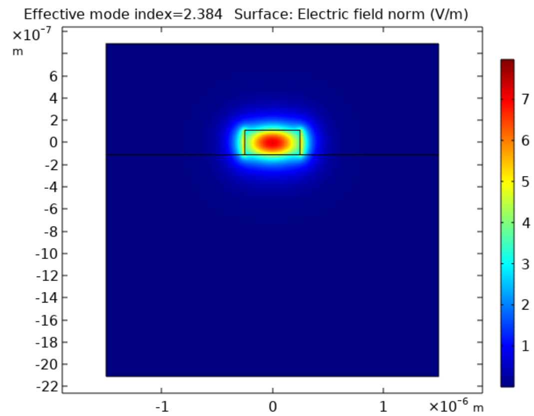

(b) 2D simulation of the cross-sectional TE mode profile of a 500 nm x 220 nm waveguide. The upper cladding is air and the substrate is SiO_2. The n_{eff} value is 2.384.

Figure 5.1: 2D BMA simulation of the TE mode in (a) a 450 nm x 220 nm core and (b) a 500 nm x 220 nm core.

In Figure 5.2 the difference between the air cladding and the rest are easily noticed. Naturally, the water and heavy water claddings are very similar due to their almost identical RI; however, another important difference is with the use of a 1.31 μm wavelength and a water cladding. The n_{eff} value when using this wavelength has a negligible extinction coefficient due to water being much less absorptive at this wavelength. Ideally using this wavelength for the TM mode with a Silicon core would yield the best results.

Figure 5.3 shows the 3D model BMAs with various cladding materials. As seen in Figures 5.2 and 5.3, the TM mode is concentrated mainly along the outer borders of the waveguide.

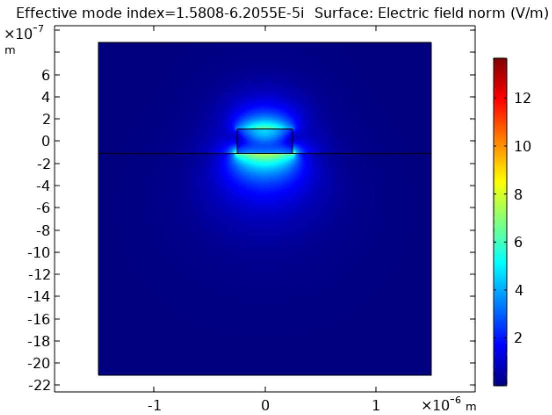

(a) Air upper cladding, wavelength 1.55 μm. n_{eff} = 1.5808-6.2055E-5i

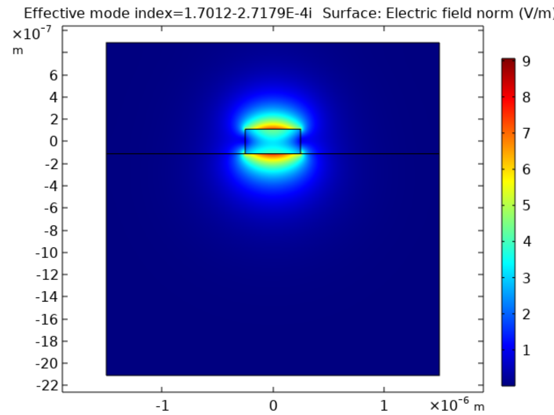

(b) H_2O upper cladding, wavelength 1.55 μm. n_{eff} = 1.7012 - 2.7179E-4i

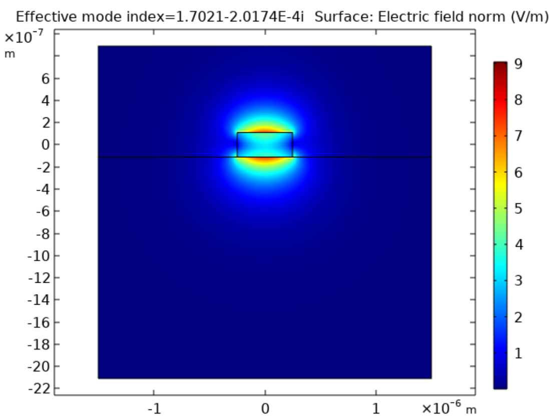

(c) D_2O upper cladding, wavelength 1.55 μm. n_{eff} = 1.7021 - 2.017E-4i

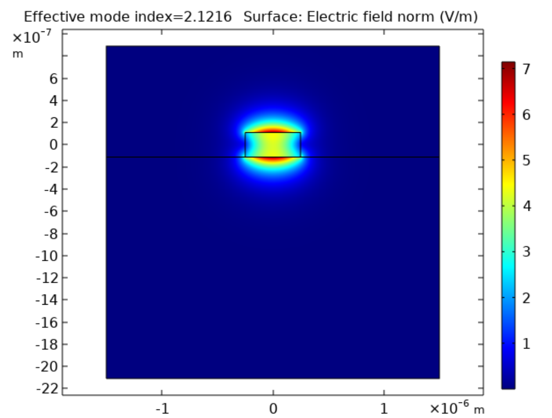

(d) H_2O upper cladding, wavelength 1.31 μm. n_{eff} = 2.1216

Figure 5.2: 2D simulations of the cross-sectional TM mode profiles of a 500 nm x 220 nm waveguide with varying cladding materials.

Due to this phenomenon, the modes tend to have higher loss in comparison to TE modes due to traveling in the lossier outer mediums. This is reflected in the exintction coefficient, k, from the n_{eff} term. The higher the value of k, the higher propagation loss the mode encounters.

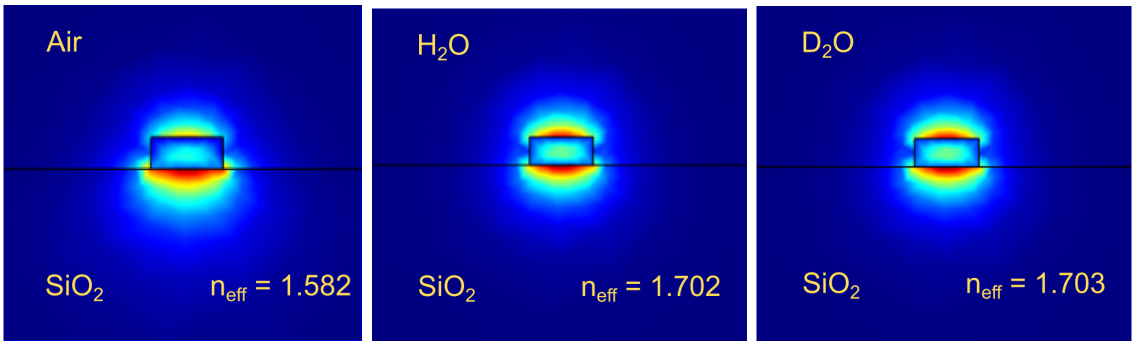

(a) TM boundary mode profile with an air cladding. **(b)** TM boundary mode profile with an H_2O cladding. **(c)** TM boundary mode profile with a D_2O cladding.

Figure 5.3: Boundary mode profiles of the TM modes of a 500 nm x 220 nm waveguide core with various upper cladding mediums.

Cladding	n$_{eff}$ (2D)	n$_{eff}$ (3D)
Air	1.5808 - 6.205E-5i	1.5825 - 9.595E-5i
H_2O	1.7012 - 2.718E-4i	1.7020 - 4.462E-4i
D_2O	1.7021 - 2.017E-4i	1.7028 - 3.827E-4i

Table 5.1: Effective index values of TM mode rings from 2D cross-sectional simulations compared to values from the full 3D model.

Table 5.1 compares the n$_{eff}$ values from the 2D simulations to the 3D models' BMA results. The real part, n, from the 3D model is very close to that of the 2D simulation, and the extinction coefficient, k, stays relatively close as well. The effective mode index from the 2D simulation is likely more accurate, because the mesh is a much higher quality.

5.1.2 TE Mode 5 μm Radius Ring

The TE mode 5 μm radius model presented here uses a 450 nm x 220 nm Silicon core and a 200 nm gap. To confirm the accuracy of the FEM model, replications of both simulated and experimental results from literature were attempted. These dimensions are based on the proposed configuration by Bogaerts et al [39]. The results were also compared with results from experimentally measured data of ADMRs with the same radius. The wavelength resolution for this simulation is 0.035 nm.

For a TE mode ring with an OPL of 70 μm and a power attenuation coefficient, α, of 2.7 dB/cm, the expected QF is approximately 30,000 [39]. This is calculated using either equation 3.16a or 3.16b while keeping the self-coupling coefficients and the single-pass amplitude coefficient constant. The single-pass amplitude coefficient, a, relates to the power attenuation coefficient, α, through equation 3.4a. Using equation 5.1, we can see that a 5 μm radius corresponds to an OPL of approximately 70 μm.

$$OPL = 2\pi R \cdot n_{eff} \tag{5.1}$$

The bus waveguides of the experimental ADMR by Bogaerts et al. [39] are bent in a semi-circular fashion as seen in Figure 5.4a rather than the traditional straight waveguide. Two configurations were modeled using FEM, one of which can be seen in Figure 5.4b and the other having the typical two straight bus waveguides. The results from these simulations are compared to the results in Bogaerts et al. [39] as well as some experimental data.

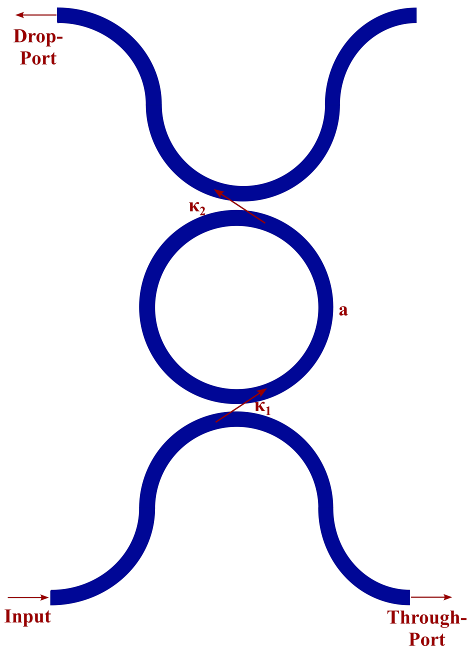

(a) Configuration tested by Bogaerts et al. [39], where the radius is 5 μm, the gap between the bus waveguides and the ring is 200 nm, and the waveguide dimensions are 450 nm wide by 220 nm thick.

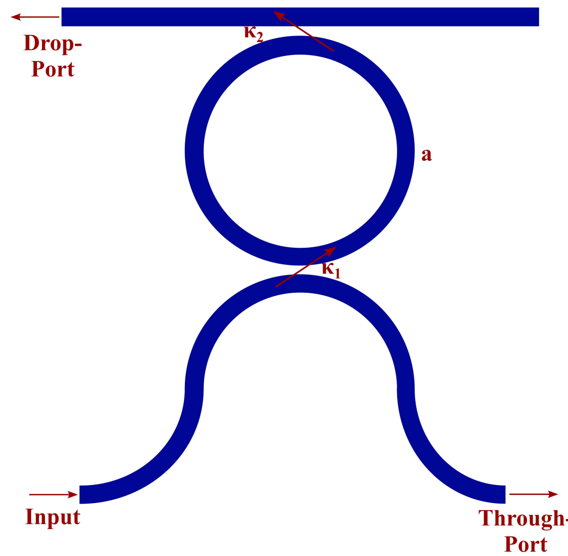

(b) Configuration tested with COMSOL that has results in Table 5.2 (Bent Input). The radius, gap, and waveguide dimensions are the same as those in (a).

Figure 5.4: Non-standard ADMR configurations tested in COMSOL.

The FEM simulation of these configurations yielded results similar to those of the simulated data, but a much larger QF is achieved compared to the experimental measurements of 8,000 from Bogaerts et al. [39]. Figure 5.5 shows the raw transmission curve of the FEM simulation with the two straight bus waveguides. The transmission in the drop-port is low, because a longer coupling length is required for the TE mode. The larger confinement factor as a result of using the TE mode is also a significant contributor to the reduced coupling into the ring, in turn, reducing the coupling coefficient and increasing the QF. The extracted QF of 33,408 corresponds to the expected value of 30,000 based on the calculations by Bogaerts et al [39]. There is a large discrepancy between the simulated QF values and the experimental result from Bogaerts et al. [39]; however, this may be due to measurement inaccuracies or structural imperfections. On the other hand, Yebo et al. [71] were able to achieve an experimentally measured QF of approximately 30,000 using the same configuration, which corresponds with the simulations. Table 5.2 compares the results the FEM simulations, results from literature, and some experimentally measured results.

An interesting effect from using the bent input waveguide resulted in more coupling of light into the ring and an increased QF. This is most likely a phenomenon that occurs at small radii as an effect of bending losses. The small bending radius causes leakage of the mode into the coupling region due to bending loss, which may help getting more of the mode to couple into the ring. The mode from the bent input waveguide may also be better matched to that inside of the ring, making coupling between the two easier as well.

Along with the quantitative transmission and QF results, several aspects of the propagated mode can be visualized throughout the structure. The most important ones that can be observed are the y-component of the electric field (E_y) and the power flow, time average in x (Poavx). Figure 5.6a shows the E_y component on-resonance. We can observe how the electric field intensity is much larger in the ring compared to the bus

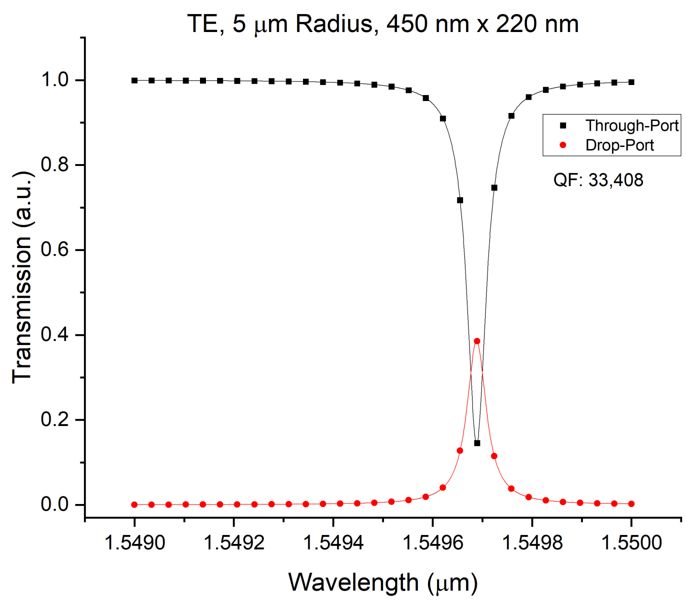

Figure 5.5: Transmission at the through-port and drop-port of a TE mode ADMR with a radius of 5 μm. The waveguide dimensions are 450 nm x 220 nm, and the gap size is 200 nm.

Core Dimensions	Radius	Gap Size	QF	Reference
450 nm x 220 nm	5 μm	200 nm	33,408	Straight Buses (FEM)
		200 nm	42,600	Bent Input (FEM)
		200 nm	~30,000	[39] (Sim.)
		~200 nm	30,000	[71] (Exp.)
		200 nm	8,000	[39] (Exp.)
500 nm x 220 nm	5 μm	200 nm	8,407	This Paper (Exp.)
		200 nm	17,908	This Paper (Exp.)
		NS	20,000	[72] (Exp.)

Table 5.2: Comparison of TE mode ring resonator configurations from literature, 3D FEM COMSOL simulations, and experimentally measured data. NS means not stated.

waveguides, because there is much more circulating power as a result of the system being in steady-state. Figure 5.6b on the other hand, shows the Poavx component, which depicts the mode's direction of propagation in the structure. In the figure, red denotes the positive x-direction and blue denotes the negative x-direction. This plot confirms that the mode is traveling in the correct direction around the ring. Similarly to the E_y plot, the Poavx component is difficult to see in the bus waveguides since most of the power is circulating in the ring. In addition, Figure 5.7 shows a full 3D view of the E_y component on the structure.

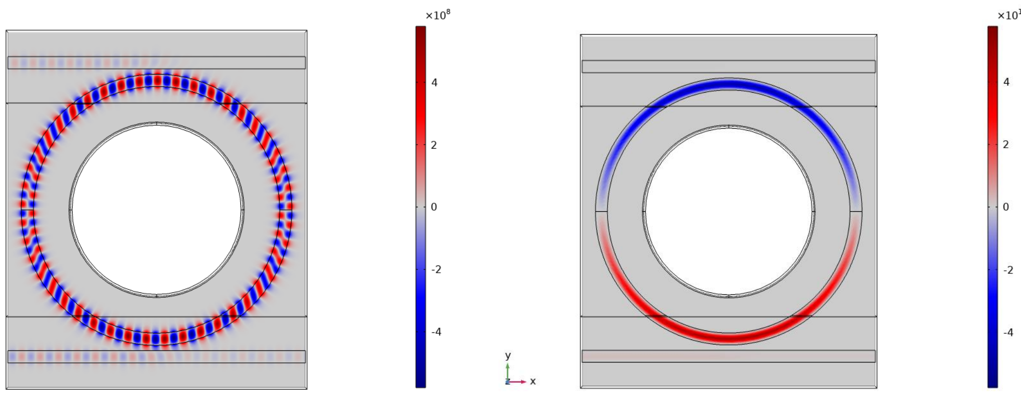

(a) E_y on resonance. **(b)** Poavx on resonance.

Figure 5.6: Top-down, cross-sectional, 3D plots of the E_y and Poavx components on and off resonance.

5.1.3 TM Mode 15 μm Radius Ring

The other main configuration tested uses the TM mode, and consists of a 15 μm radius and more typical 500 nm x 220 nm waveguide core dimensions. Using a high quality mesh for the waveguide cores and coupling regions, a 15 μm radius is the largest feasible size for

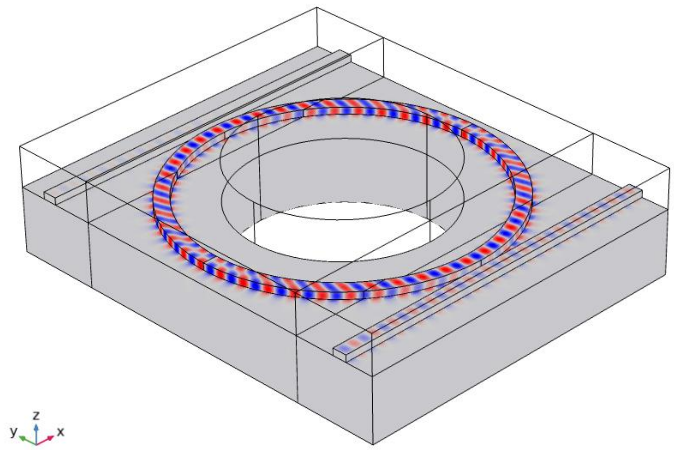

Figure 5.7: Plot showing the E_y component of the 5μm TE mode model on the on the full 3D geometry. The upper cladding is set to be transparent to observe E_y on the waveguide core.

computaions with 16 GB of RAM. To simulate a model with a larger radius or finer mesh quality, 32 GB of RAM would be necessary. The wavelength resolution for this simulation is 0.18 nm.

Similarly to the 5 μm TE mode ring, Figure 5.8 shows the transmission curve at the through-port and drop-port of this configuration with a 450 nm gap. The stark difference; however, is that the transmission obtained at the drop-port is much higher and the QF achieved is reduced significantly. The drop in QF is expected as a result of using the TM mode. The larger radius also increases the coupling as a direct result from increasing the coupling length. The use of the TM mode allows for more coupling to occur at the expense of reducing the QF. This is mainly due to weaker mode confinement and the coupling occuring over a larger range of wavelengths. Because most of the light is traveling along the outside of the waveguide, it is more susceptible to RI changes and loss mechanisms from more absorptive mediums such as water. As seen previously in equations 3.16a and 3.16b, the loss, based on the a variable, does have an effect on the resulting QF. Past studies have investigated this phenomenon - notably one by Nawrocka et al., confirms the broadening of resonance peaks in the TM mode in comparison to the TE mode [12]. Another study by Schmidt et al. focuses on the tradeoffs between the TE and TM mode for biosensors, finding that the TM mode increases sensitivity, but reduces the QF [40].

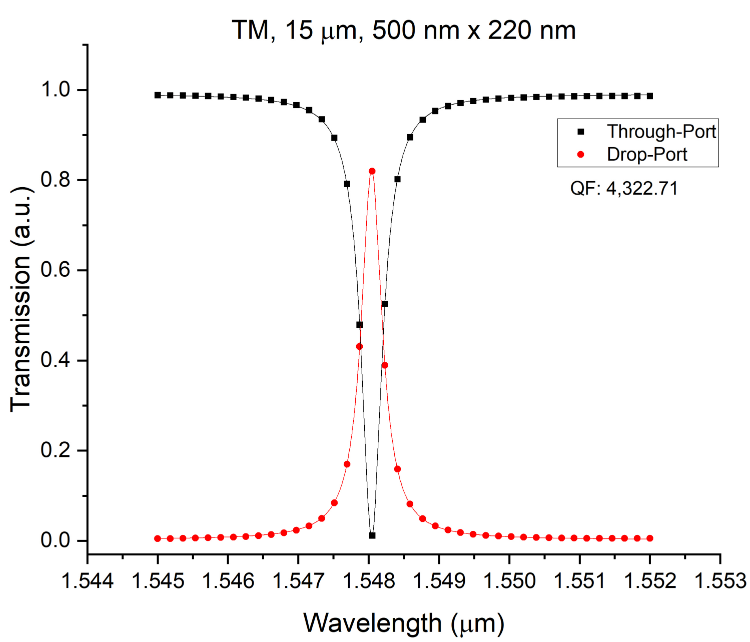

Figure 5.8: Transmission at the through-port and drop-port of a TM mode ADMR with a radius of 15 μm. The cladding is air, the waveguide dimensions are 500 nm x 220 nm, and the gap size is 450 nm.

Table 5.3 shows differences in ring configurations for TM modes from literature compared to 3D FEM simulations and experimentally measured rings. The weaker confinement of the TM mode along with it being focused on the outer walls of the waveguide core, causes the mode to be more susceptible structural imperfections and changes in refractive index. Thus surrounding media with larger extinction coefficients have a significant effect on the structure's QF. Another aspect that Table 5.3 shows is the effect of the gap size on the QF of the ring. Notably, increasing the gap size significantly increases the QF. This is caused by the QF trending towards the intrinsic QF. As the coupling decreases with gap size, so does the peak transmission on-resonance in the drop-port. This in turn reduces the FWHM to increase the QF towards Q_i.

<table>
<tr><th>Core Dimensions</th><th>Radius</th><th>Gap Size</th><th>QF</th><th>Reference</th></tr>
<tr><td>500 nm x 150 nm</td><td>40 μm</td><td>NS</td><td>1,914</td><td>[40] (Exp.)</td></tr>
<tr><td rowspan="11">500 nm x 220 nm</td><td>40 μm</td><td>NS</td><td>9,200</td><td>[40] (Exp.)</td></tr>
<tr><td rowspan="9">15 μm</td><td>300 nm</td><td>1,294</td><td>This Paper (FEM)</td></tr>
<tr><td>350 nm</td><td>1,858</td><td>This Paper (FEM)</td></tr>
<tr><td>400 nm</td><td>2,678</td><td>This Paper (FEM)</td></tr>
<tr><td>425 nm</td><td>3,368</td><td>This Paper (FEM)</td></tr>
<tr><td>450 nm</td><td>4,323</td><td>This Paper (FEM)</td></tr>
<tr><td>475 nm</td><td>5,408</td><td>This Paper (FEM)</td></tr>
<tr><td rowspan="3">200 nm</td><td>504</td><td>This Paper (Exp.)</td></tr>
<tr><td>723</td><td>This Paper (Exp.)</td></tr>
<tr><td>844</td><td>This Paper (Exp.)</td></tr>
</table>

Table 5.3: Comparison of TM mode ring resonator configurations from literature, 3D FEM COMSOL simulations, and experimentally measured data. NS means not stated in the literature.

Figures 5.9a and 5.9b depict the z-component of the electric field (E_z) on resonance and the Poavx on resonance, respectively. In comparison to the TE mode, the electric field intensity in the drop-port's waveguide is much clearer due to the increased coupling. The Poavx plot is used to confirm that the mode is propagating in the correct direction, where blue denotes the negative x-direction and red denotes the positive x-direction.

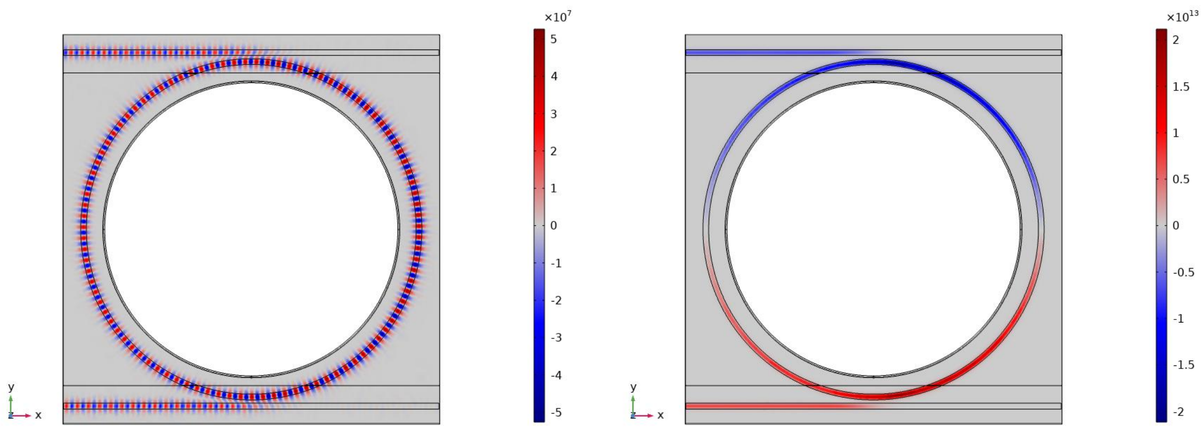

(a) E_z on resonance. **(b)** Poavx on resonance.

Figure 5.9: Top-down, cross-sectional, 3D plots of the E_z and Poavx components on resonance.

Figure 5.10 shows the resonance peak at the drop-port of this configuration with different cladding materials. As expected, it is clear that the increasing RI of the cladding medium has a direct correlation with the shift of the resonance peak. The shift from air to water is approximately 1 nm, whereas the shift from air to heavy water is approximately 1.5 nm.

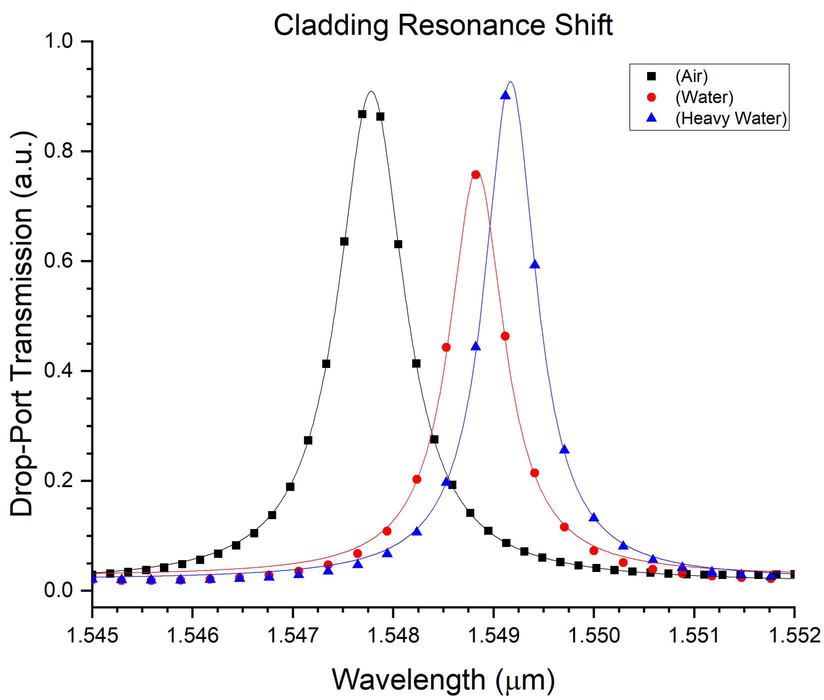

Figure 5.10: Shift in the resonance peak at the drop-port of a TM mode ADMR with a radius of 15 μm, 500 nm x 220 nm core, and a 350 nm gap.

5.1.4 Effect of Meshing Quality on Results

The mesh quality of the model has a significant impact on the quality of the results up to a certain maximum mesh size. As expected, reducing the maximum size of each meshing element increases the quality of the results. This can be observed by running simulations using increasing mesh quality, and generating a convergence plot of the ring's quality factor versus the maximum mesh element size. The maximum mesh element sizes are changed for only the ring and the bus waveguides as they are the main regions of interest.

A convergence plot was made to show the relationship between the maximum mesh element size and the resulting quality factor. For a ring with a 15 μm radius and core dimensions of 540 nm (width) by 220 nm (height), the quality factor versus maximum mesh size plot can be seen in Figure 5.11. There is a noticeable trend where the quality factor begins to drastically decrease after mesh elements begin to increase past the 150 nm size. The most likely explanations for the QF to decrease slightly after the 150 nm size are that the mesh may less more uniform and slightly worse for computations, or the mode may be better matched at the 150 nm mesh size. The decrease in quality factor at the finest mesh size (100 nm) may be also be due to performance issues affecting the simulation results. When simulating other structures such as racetrack resonators, a new convergence plot should be generated; however, the results will likely follow a similar relationship. For a waveguide core of 500 nm x 220 nm, the ideal maximum mesh size is in the range of 110 nm to 125 nm for the best blend of accuracy and performance.

The computational complexity of the simulation is also evaluated by observing the change in simulation time in relation to the amount of meshing elements and degrees of freedom (DoF) in the model. The models are simulated on a system with an Intel©Core$^{\text{TM}}$ i7-10750H CPU and 16 GB of RAM. Increasing the amount of RAM should both speed up simulation times and allow for larger and more complex models to be simulated. Table 5.4 shows the relationship between simulation time and the model complexity, defined by the amount of mesh elements and DoF. The first 5 μm entry uses a slightly lower mesh quality (core: 115

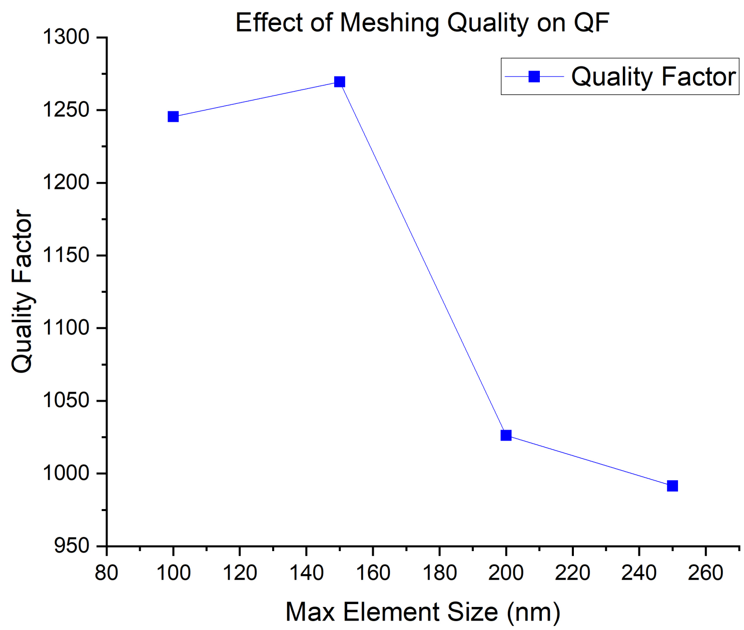

Figure 5.11: Plot of the quality factor versus the maximum mesh element size. The models were simulated using a wavelength around 1550 nm.

nm max, ring: 125 nm max) than the second entry (core: 100 nm max, ring: 115 nm max). The third entry of 15 μm uses the same meshing quality as the second entry. Each entry in Table 5.4 was simulated for 30 discrete points in a wavelength sweep. It is clear that increasing the mesh quality and the size of the model have a significant impact on the computational complexity. Doubling the number of mesh elements by increasing the radius from 5 μm to 15 μm causes the simulation time to more than triple.

Radius	DoF	DE	BE	EE	Simulation Time
5 μm	1,138,867	168,607	18,358	2,427	118 min
5 μm	1,395,307	207,670	21,249	2,531	150 min
15 μm	3,041,365	461,788	52,632	5,601	510 min

Table 5.4: Comparison between the amount of mesh elements and the simulation time of the model (DoF - Degrees of Freedom, DE - Domain Elements, BE - Boundary Elements, EE - Edge Elements).

5.1.5 Coupling and Loss Coefficients

Important relationships between the system's parameters can be determined by plotting them against each other. First, the extinction coefficient from n_{eff} is directly correlated with the power attenuation coefficient, α. Figure 5.12 shows how α and k are directly proportional to each other when changing only the cladding material. Assuming a linear relationship holds, an estimate for a, the single-pass amplitude coefficient, can be made to use for an analytical model. However, this would only work for a specific configuration as the n_{eff} changes based on core dimensions, wavelength, materials, and the polarization.

As previously mentioned, the waveguide loss due to sidewall roughness can also be accounted for by using a custom silicon material definition. For example, a 5 μm radius ADMR in air is simulated with two different loss values: 1.5 dB/cm, which is measured by ANT Inc. [73], and a significantly larger value of 10 dB/cm to observe clear differences in the results. Figure 5.13 shows the difference in transmission at the drop port for the ADMR with each waveguide loss value. As expected, the transmission decreases significantly when a high loss is present.

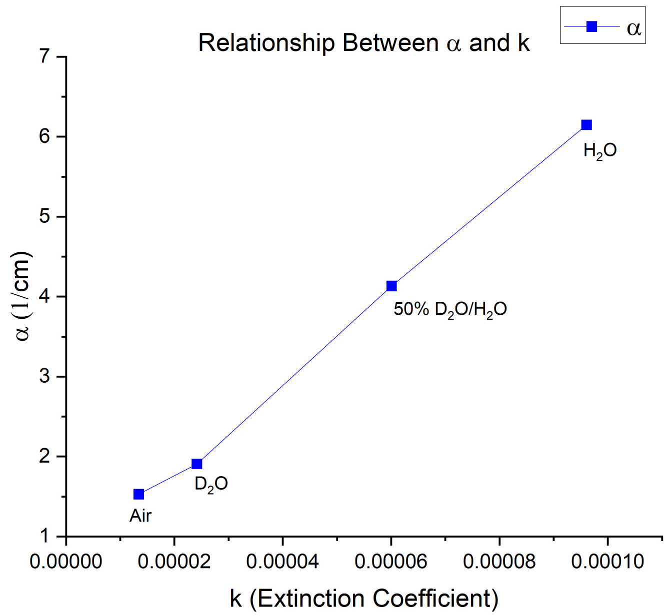

Figure 5.12: The relationship between α and k with differing cladding materials. The ADMR has a 15 μm radius, 500 x 220 nm Si core, and 2 μm thick SiO_2 substrate.

For the TE mode, large variations in the QF can be observed as a result of losses due to sidewall roughness. There is a 16.1% decrease in the QF when increasing the loss from 0 dB/cm to 1.5 dB/cm, and a 28.8% decrease in QF when increasing the loss from 0 dB/cm to 10 dB/cm. Therefore, simulating the structure with even small random loss values, for example, up to 2.5 dB/cm, we can expect QF variations of up to approximately 18.4%. In comparison, the variations of measured QFs in the results from Bogaerts et al. for a TE mode ADMR with a 250 nm gap are approximately 20% [39]. In contrast, the QF variations in the TM mode are significantly smaller. Increasing the loss from 0 dB/cm to 1.5 dB/cm only decreases the QF by approximately 0.5%.

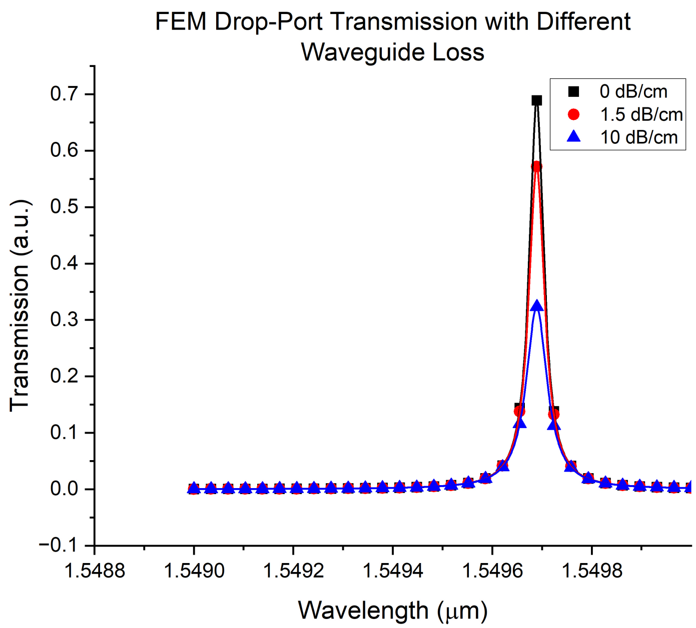

Figure 5.13: Difference in simulated drop-port transmission when using a custom silicon material that estimates loss due to sidewall roughness.

Another important relationship for generating an analytical model is that between κ, the cross-coupling coefficient, and the coupling gap distance. Figure 5.14 shows the relationship between κ and the gap size for the 15 μm radius model. Similarly to the relationship between α and k, this relationship only holds for this specific configuration. The equations used for analytical models (3.13a, 3.13b) do not account for gap size, but are dependent on the cross-coupling coefficient, κ. Using this relationship would be important for determining the gap size from an analytical model; however, it would only apply to a specific radius - in this case 15 μm. This is due to the fact that changing the radius directly affects the coupling length, in turn affecting the coupling coefficients - as radius goes to infinity, so does coupling length.

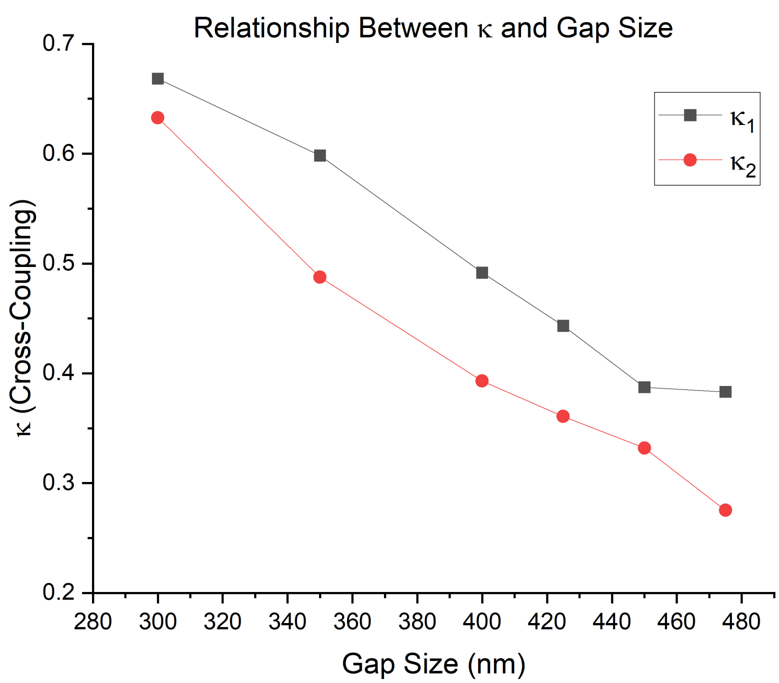

Figure 5.14: The relationship between κ and the gap size between the bus waveguides and the ring. The ADMR has a 15 μm radius, 500 x 220 nm Si core, and 2 μm thick SiO_2 substrate. The cladding medium is air at all points.

5.1.6 Quality Factor

The QF is dependent on multiple elements, including the gap size. Figure 5.15 shows the relationship between the QF and the gap size for an ADMR with a 15 μm radius in the TM mode based on the FEM results. An exponential relationship can be observed in this relationship, where as the gap size increases, the QF approaches the intrinsic QF. This relates directly to the concept of the intrinsic QF, Q_i, which is the QF when the ring is isolated from any coupler. Thus, no losses from coupling in and out of the ring are considered, which increases the QF significantly. Equations 5.2a and 5.2b define the total QF, Q_t, in terms of the intrinsic QF, Q_i, and the coupling QF, Q_c [1, 52]. In equation 5.2b, L_{rt} refers to the round-trip length of the ring, and t refers to the transmission coefficient.

$$\frac{1}{Q_t} = \frac{1}{Q_c} + \frac{1}{Q_i} \tag{5.2a}$$

$$Q_i = \frac{2\pi n_g}{\lambda\alpha}, \quad Q_c = \frac{\pi L_{rt} n_g}{\lambda \log_e |t|} \tag{5.2b}$$

The Q_i was simulated using the eigenfrequency method, while utilizing the 3D FEM model. This process involves finding the resonant frequency when the system has no driving force, in this case, the input waveguide. The resulting Q_i values for a ring with a 15 μm radius surrounded by various upper cladding materials can be seen in Table 5.5. Chrostowski et al. [1] investigated the Q_i values versus experimentally measured QFs for TE and TM rings, with results included in Table 5.5. The radii for these rings are not stated in the study. In Table 5.5, we can observe the effect of losses from the use of media with higher absorption losses such as water. The extinction coefficient of water being $1.492 \cdot 10^{-4}$ at a wavelength of 1.55 μm [74] is approximately 3,240% larger than that of heavy water. This causes the Q_i of the MRR in water to decrease by 2,426% in comparison to that of the MRR in heavy water.

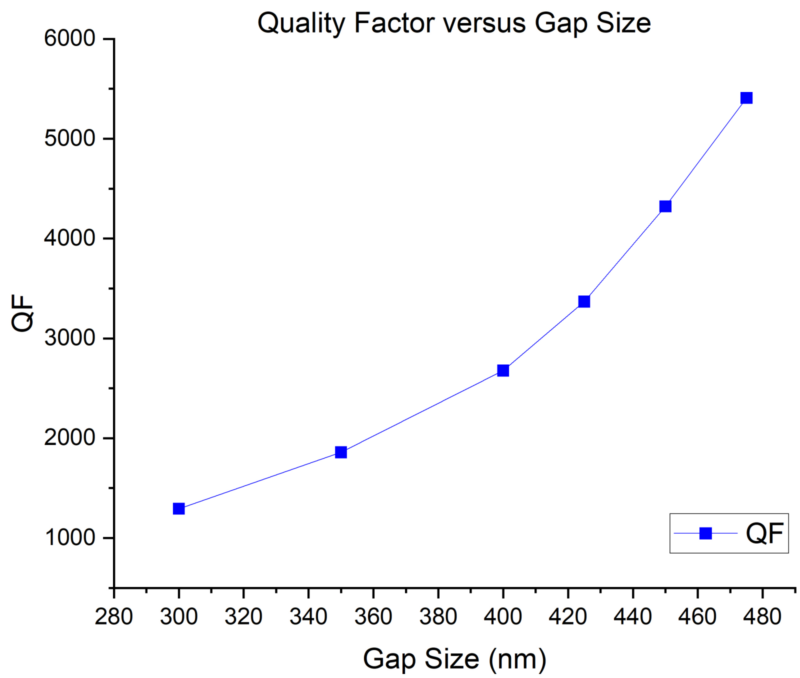

Figure 5.15: Relationship between the QF and the gap size for an ADMR with a 15 μm radius in the TM mode. These results are taken from FEM simulations.

In addition, from the study by Chrostowski et al., we can observe how the TM mode also reduces the Q_i due to the mode being more susceptible to the high absorption coefficient of water. From Figure 5.15 and Table 5.5 we can observe how as the gap size increases, the effect of the Q_i term in equation 5.2a becomes slightly more prominent. By inserting values of Q_t and Q_i into equation 5.2a, we can calculate the expected value of Q_c. Using much larger gap sizes would be required to see a more noticeable change in Q_c. Using an exponential fit function on the curve from Figure 5.15 to generate equation 5.3, where A is 26.365, R_0 is 0.011, and QF_0 is 596, the gap size necessary for a given QF can be approximated. By doing this, we can observe how large the required gap size is for Q_i to have a more significant effect on Q_t. For example, for the QF of the ADMR to reach the Q_i of $8.6 \cdot 10^6$, the gap size would have to be approximately 1.15 μm.

$$QF = QF_0 + A \cdot e^{R_0 \cdot x} \tag{5.3}$$

Cladding Material	n	k	Q_i	Reference
Air	1.0003	-	8,608,000	This paper (FEM)
Heavy Water	1.317	$4.465 \cdot 10^{-6}$	2,875,700	This paper (FEM)
Water	1.3154	$1.492 \cdot 10^{-4}$	113,830	This paper (FEM)
			106,719	[1] (TE)
			34,500	[1] (TM)

Table 5.5: Table containing Q_i results from FEM and literature along with refractive index values for each medium. Losses for the TE and TM rings from [1] are 6.9 dB/cm and 22.7 dB/cm, respectively.

Using the relationship in equation 5.3, an estimation for the simulated QF with a gap size of 200 nm can be made. The expected simulated QF at a gap size of 200 nm is approximately 834, corresponding to the largest QF of the measured ring included in Table 5.3, being 844.

As we increase the coupling gap size, the QF will increase; however, the system also ventures into the under-coupled regime after a certain point. Most commonly, this point occurs at the wavelength at which the resonance peak begins to decrease. A slightly under-coupled ring is desired due to having a higher QF than a critically-coupled ring; however, having the ring be too under-coupled leads to a smaller SNR. Larger QFs are important for sensitivity, but maintaining a large SNR is important as well for the ability to discern resonance peaks from noise.

5.2 Experimental Measurements

5.2.1 Fabrication Details

Two configurations of MRRs were measured: one with a 5 μm radius and the other with a 15 μm radius. Both rings have core dimensions of 500 nm x 220 nm, and were measured in the TM mode. The MRRs were fabricated by ANT Inc. Technology through the CMC multi-project wafer fabrication run. This process involves using a 100 keV electron beam lithography system to create a 220 nm thick silicon film on top of a 2,000 nm BOX [69].

5.2.2 Measurement Process

A tunable laser source was used to sweep through wavelengths in the C-band (infrared) to obtain resonance peaks in this range. A wavelength range of 1.515 μm to 1.595 μm was swept for the 5 μm radius ring and a range of 1.54 μm to 1.582 μm was swept for the 15 μm radius ring. Transmission at the through-ports and drop-ports were measured using an optical spectrum analyzer. A fiber alignment unit (FAU) was used to align the optical fibers with the grating couplers at the through-port, drop-port, and input port. The wavelength resolution for the 5 μm radius rings is 0.05 nm. The wavelength resolution for the 15 μm radius ring is 0.01 nm. For the simulation of the TM mode 5 μm radius ring, the wavelength resolution is 0.41 nm.

5.2.3 Experimentally Measured TM Mode Rings

A 5 μm radius ring was tested in the TM mode, and the results were compared to a FEM simulation of the same configuration. Figure 5.16 shows the transmission curve from the FEM simulation of this ADMR. There is a stark difference in comparison to the TE mode, where the resonance peak here has broadened significantly. This in turn greatly decreases the QF - approximately by a factor of 100. The QF achieved with the simulation is 391. Although extremely small, this QF value is to be expected for the TM mode at such a small radius and coupling gap.

The experimental results of this configuration are shown in Figure 5.17. The position of the resonance peaks do not line up perfectly with the FEM result; however, the QF values remain very similar, the largest being 363. Having comparable results with the simulation of this configuration, these results further confirm the accuracy of the 3D FEM model.

Figure 5.18 shows the resonance peak of the FEM result overlaid onto that of the experimentally measured ring. The spectra of the experimental ring are baseline corrected using a polynomial fit function and normalized to the fit arbitrary unit scale. We can notice a strong similarity between the overall shape of the transmission curves.

In addition, the same ring was measured after covering it with water. The transmission at

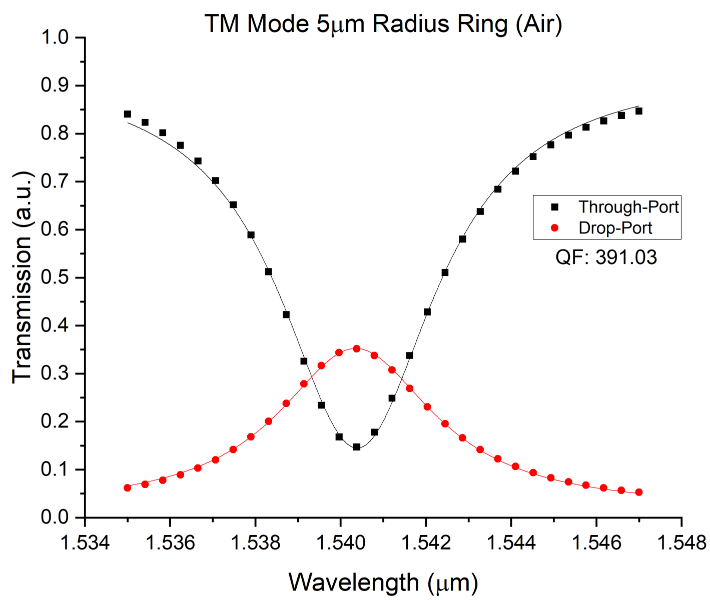

Figure 5.16: FEM-simulated transmission at the through-port and drop port of the 5 μm radius TM mode ring. The core dimensions are 500 nm x 220 nm and the gap size is 200 nm.

the through-port and drop-port of the ring in water is shown in Figure 5.19. The QF values here are slightly higher than both the simulated and experimentally measured ring in air; however, this is caused by the grating coupler also being covered with water. Being designed for an air cladding, the transmission through the grating coupler in water is reduced, also lowering the transmission through the ring. Therefore, the FWHM of the resonance peaks are reduced, increasing the QF. The right-most resonance peak in Figure 5.19 is also partially cut off, which reduced the FWHM, increasing the QF slightly.

An ADMR with a 15 μm radius in the TM mode was also measured and compared with

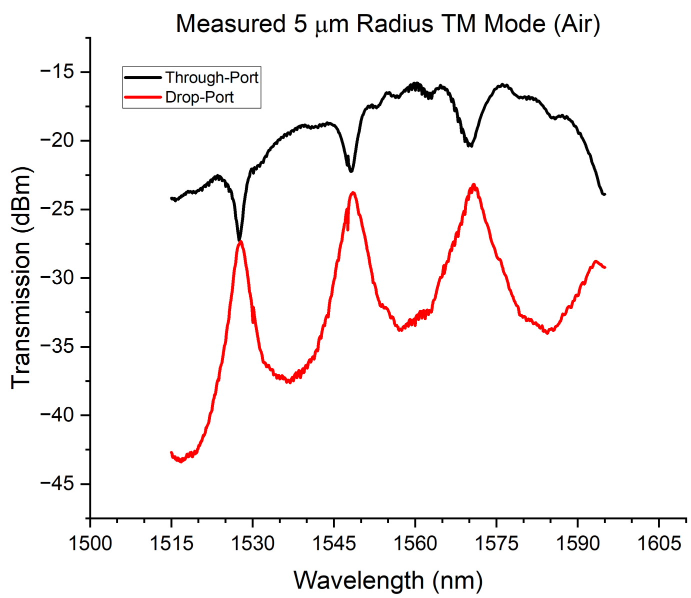

Figure 5.17: Experimental results for a TM mode 5 μm radius ring in air. The QF values of the drop-port from left to right are 363, 258, 171.

simulation results. Figure 5.20 shows the measured transmission curve of this ring over a wavelength range of 1.54 μm to 1.58 μm. From this plot, the FSR is approximately 7.1 nm.

5.3 Analytical Simulations

After extracting the self-coupling, cross-coupling, and single-pass amplitude coefficients (t, κ, a) from the COMSOL simulation, the analytical model is computed in MATLAB. An estimation of n_{eff} is made over a range of wavelengths using the change in n_{eff} over the change in wavelength. This is done by performing a linear fit of the real part of $\mathrm{n_{eff}}$ and applying the equation to an array of wavelengths. All of the remaining parameters are

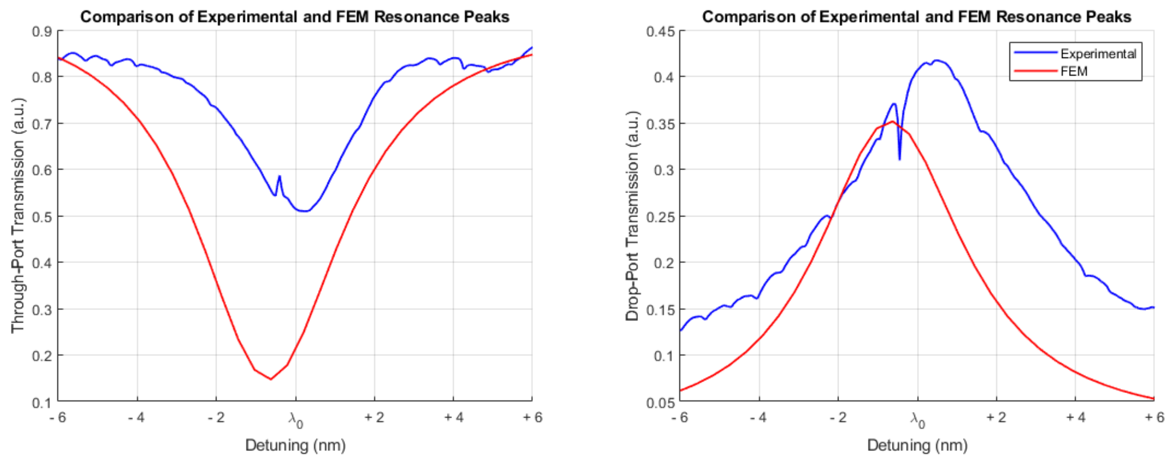

(a) Through-port transmission.

(b) Drop-port transmission.

Figure 5.18: Comparison of the resonance peak from the FEM simulation and the experimentally measured ring in air with a 5 μm radius. The spectra are plotted relative to their respective center resonance wavelength.

inserted into equations 3.13a and 3.13b, and the power (P_{t1} and P_{t2}) are plotted over wavelength. This provides an accurate depiction of the transmission curve over a larger range of wavelengths than the one computed in COMSOL. When compared to experimental results, the analytical model accurately predicts the FSR within a ± 1 nm range. Although the peak locations may not line up with those from the 3D FEM model, the QF values are similar to both the FEM results and the experimental ring.

Figure 5.21 shows the resulting analytical model for an ADMR with a 15 μm radius and 450 nm gap with air cladding. The extracted coefficients from the COMSOL model are as follows: $t_1 = 0.919447, t_2 = 0.945065$, and $a = 0.988863$. The FSR is observed to be approximately 7.3 nm for the ring with a 15 μm radius. This value is very close to that of

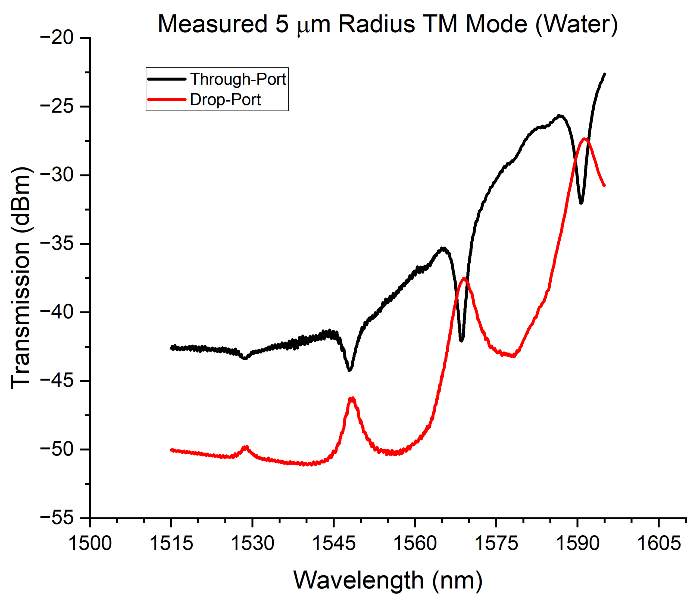

Figure 5.19: Experimental results for a TM mode, 5 μm radius ring in water. The QF values of the drop-port from left to right are 460, 343, 423.

the experimentally measured FSR of this configuration being 7.1 nm.

Applying the same process to the 5 μm radius ring in the TM mode, the analytical model generated is shown in Figure 5.22. The extracted coefficients from the FEM model are as follows: $t_1 = 0.787889, t_2 = 0.780322$, and $a = 0.735672$. These values are much smaller compared to the coefficients from the 15 μm radius model above. The main contributor to this is the decreased radius. The ring with a 5 μm radius suffers significantly from bending losses due to the relatively small bending radius. This effect can be seen when comparing the a values. In Figure 5.22, the observed FSR is approximately 21.8 nm. This value is almost the same as the experimental result's FSR of approximately 20.8 nm.

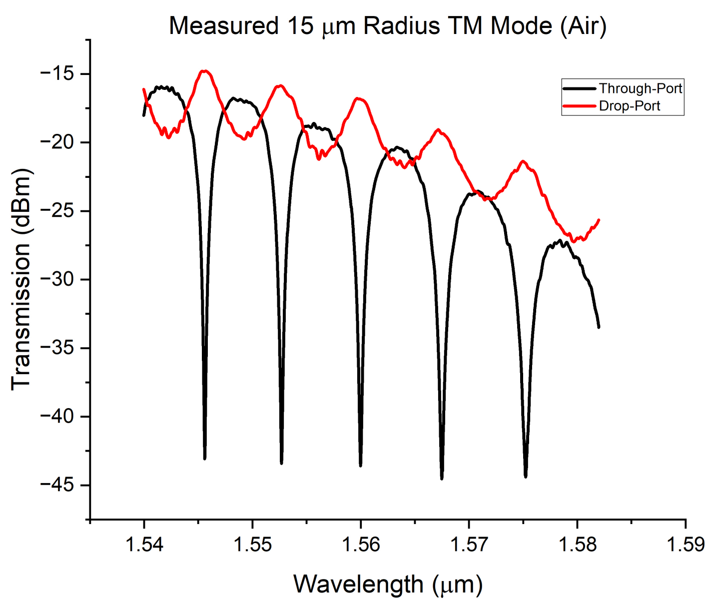

Figure 5.20: Experimental results for a TM mode, 15 μm radius ring with an air cladding. The first three QF values of the drop-port from left to right are 504, 501, and 501.

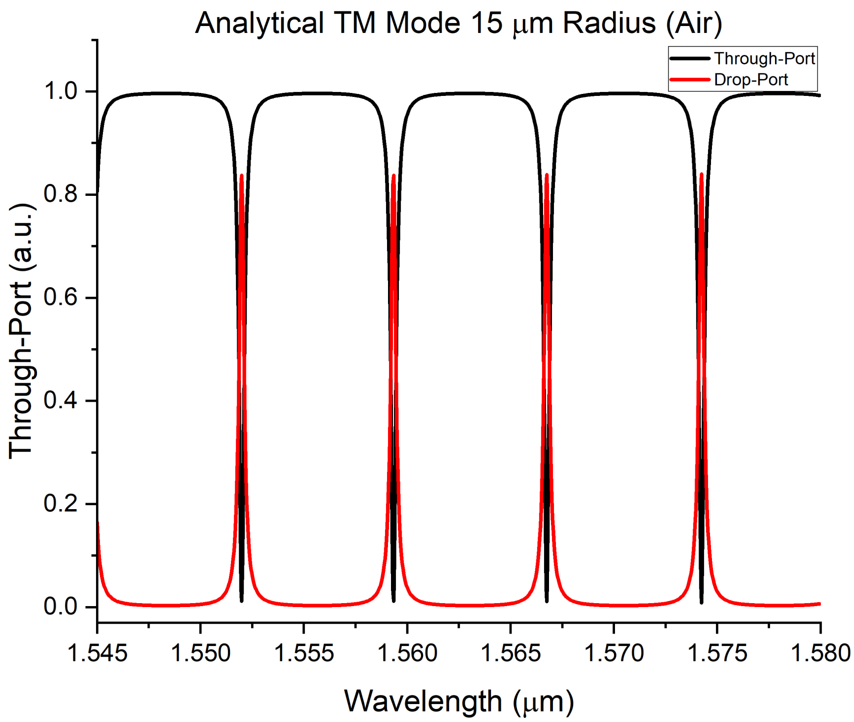

Figure 5.21: Analytical model of an ADMR based on the coefficients extracted from the COMSOL model. The ring is in the TM mode and has a 15 μm radius, 450 nm gap, and air cladding.

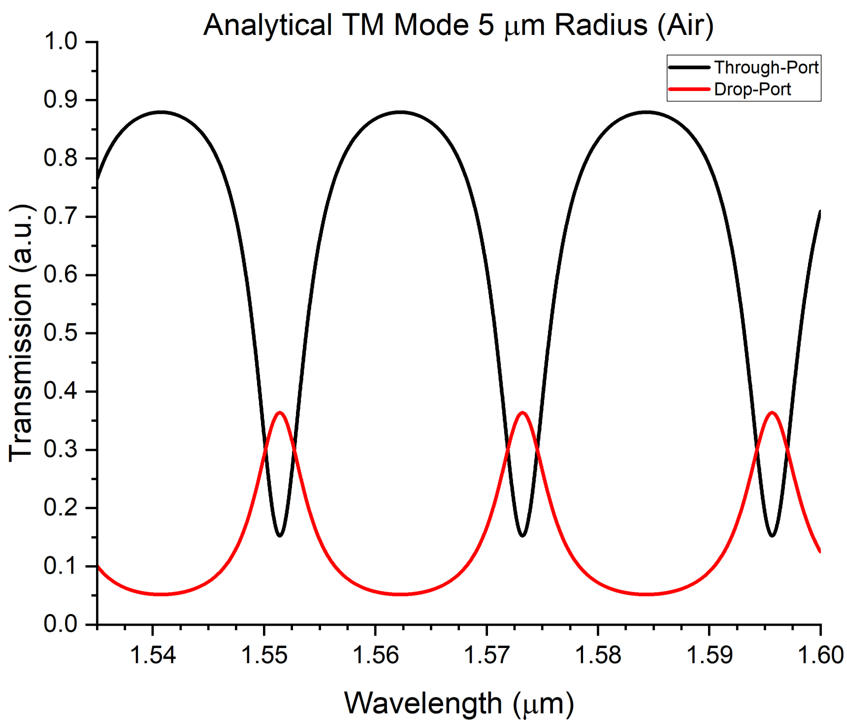

Figure 5.22: Analytical model of an ADMR based on the coefficients extracted from the FEM model. The ring is in the TM mode with a radius of 5 μm, 200 nm gap, and an air cladding.

Chapter 6

Conclusion

This thesis presents a very accurate, fully 3D, FEM simulation of an ADMR in various configurations, and it is backed up with an analytical model to provide a larger range of results. The 3D simulation results are compared to both results from literature and experimental measurements to confirm the accuracy of the FEM model. Although the QFs in the TM mode are not high, ranging from 390 at the worst to approximately 5,000 at best, these values correspond well with experimental results. The simulated QF of the TM mode ring with a 5μm radius being 391 is just 7.713% larger than the best QF of the experimental ring at 363. In addition, the FSR values extracted from the analytical models correspond with those of the experimentally measured values. For the 5 μm radius ring in the TM mode, the simulated FSR is approximately 21.8 nm, which is just 1 nm off the 20.8 nm FSR of the experimentally measured ring. The simulated TE mode configuration modeled after the proposed design by Bogaerts et al. [39] corresponds with their expected calculations. The FEM model produced a QF of 33,000 whereas the expected QF was approximately 30,000. Although the simulated QF was much larger than the measured 8,000 QF [39], it corresponds with the measured QF of 30,000 from the study by Yebo et al [71].

Since COMSOL currently does not support GPUs for parallel processing, the significant computational power required to run these simulations hinders the ability to accurately model larger configurations with consumer-rated computers. For a device with 16 GB of RAM, an ADMR with a 15 μm radius is the maximum size able to produce accurate results. When keeping a constant mesh quality, increasing the size of the model from a 5 μm radius to 15 μm doubles the number of mesh elements, and in turn, increases the simulation time by 240%. To simulate ADMRs with a radius such as 30 μm and the same mesh quality, 32 GB of RAM would be required. For radii above 30 μm, 64 GB of RAM may be required while keeping the meshing quality constant; however, at that size the mesh quality could likely be reduced in some regions.

A few relationships from the simulations were also analyzed, notably that between the QF and the gap size. The exponential increase in the QF as the gap size increases, correlates with the established fact that the QF approaches the intrinsic quality factor Q_i as the ring becomes completely isolated. On the other hand, the cross-coupling coefficient, κ, decreases as the gap size increases, showing the direct correlation that κ has with the gap size. Finally, the extracted power attenuation coefficient of the ring, α, correctly correlates with varying extinction coefficients, k, from material RI values.

6.1 Future Work

The most significant aspect to be worked on in the future is the implementation of other physics modules. With this, surface functionalization of the waveguides can be accounted for along with adding particles to represent bioreceptors along the ring. Particles such as spheres with the optical properties of cells, DNA, viruses, etc. can be added to the model; however, these would ideally be replaced with more complex geometric structures to more accurately reflect the effects they have. The mesh quality for these added structures would have to be significantly finer, which will affect the computational complexity. Other potentially interesting areas to explore with this are thermal changes and electrical potentials, and observing how they affect the results.

Another part to expand upon is the coefficient extraction process. Since the process involves solving a set of polynomial equations, the computation outputs several different solutions sets. Because of this, many solutions have to be filtered out - notably non-real results and values greater than 1 or less than 0. Even after filtering out all these solutions, two sets remain; however, when inserted into the analytical model, they yield the same resulting plot.

Chapter 7

Appendix

COMSOL model files and an instruction manual containing details about how to create the model have been uploaded to the McGill Dataverse. The following links contain the McGill Dataverse repository and the official COMSOL Wave Optics user manual.

- McGill Dataverse repository: https://doi.org/10.5683/SP3/S17UTL
- COMSOL EWBE user manual:
  https://doc.comsol.com/6.0/doc/com.comsol.help.woptics/WaveOpticsModuleUsersGuide.pdf

Wavelength	Material	n	k	Reference
1.55 μm	Si	3.4757	-	[49]
	SiO_2	1.4440	-	[75]
	H_2O	1.3154	$1.4925 \cdot 10^{-4}$	[74]
	D_2O	1.3170	$4.4651 \cdot 10^{-6}$	[74]
	Air	1.0003	-	[76]

Table A. 1: Table of refractive indices used for materials in the FEM simulations discussed in this paper.

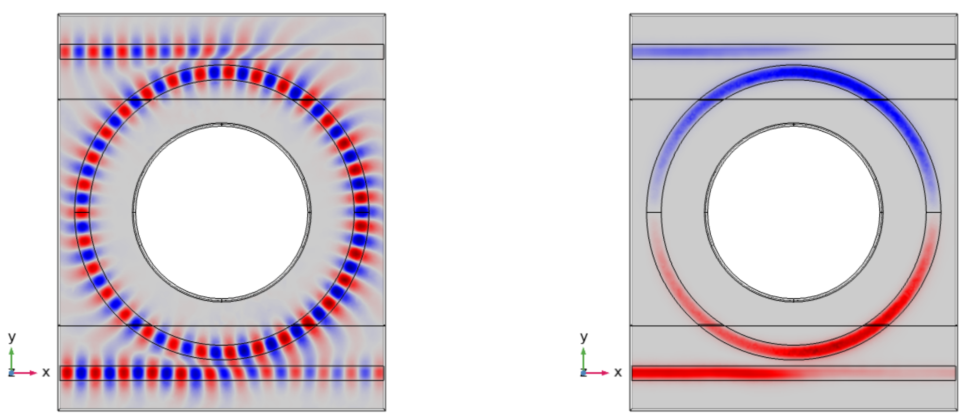

(a) E_z on resonance. **(b)** Poavx on resonance.

Figure A.1: TM mode, 5μm radius, 500 nm x 220 nm core, air cladding. Top-down, cross-sectional, 3D plots of the E_z and Poavx components on resonance.

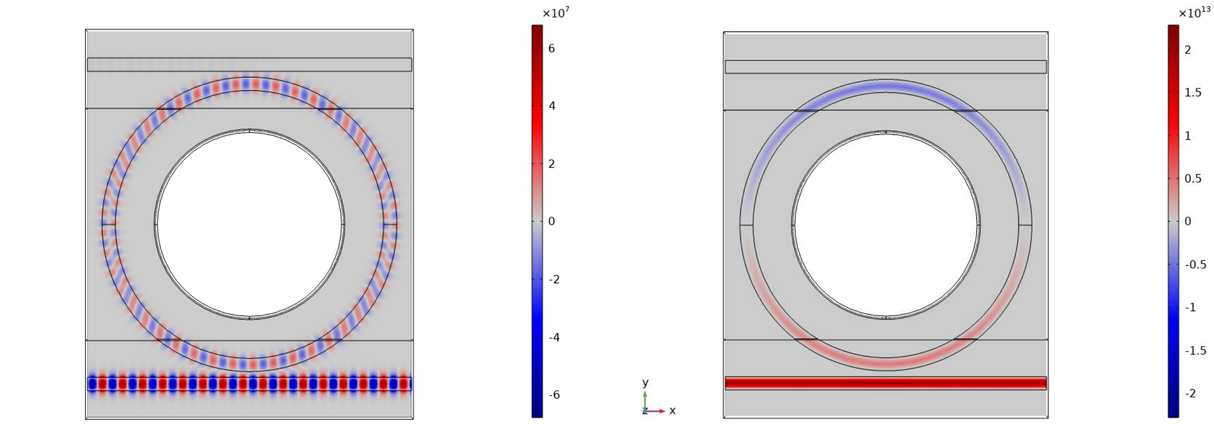

(a) E_y off resonance. **(b)** Poavx off resonance.

Figure A.2: TE mode, 5 μm radius ring with an air cladding. Top-down, cross-sectional, 3D plots of the E_y and Poavx component on and off resonance.

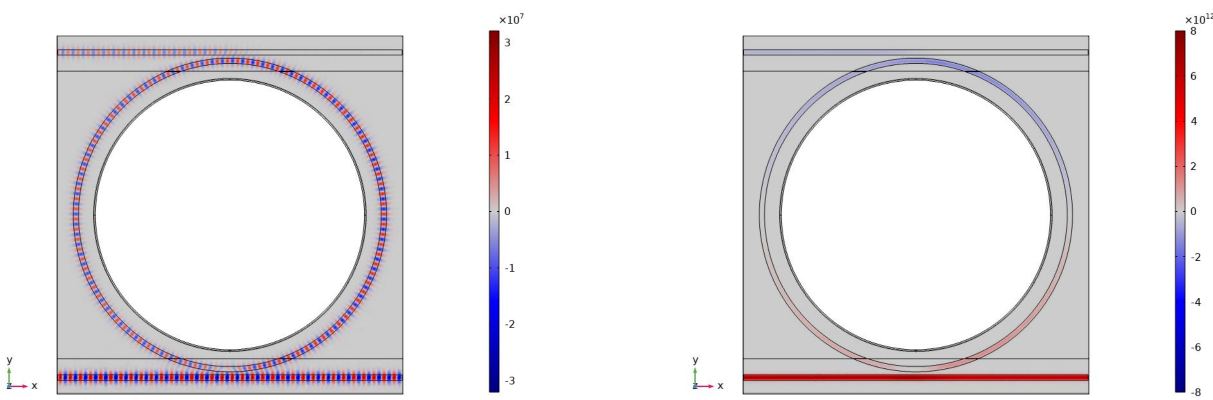

(a) E_z off resonance. **(b)** Poavx off resonance.

Figure A.3: TM mode, 15 μm radius ring with an air cladding. Top-down, cross-sectional, 3D plots of the E_z and Poavx component on and off resonance.

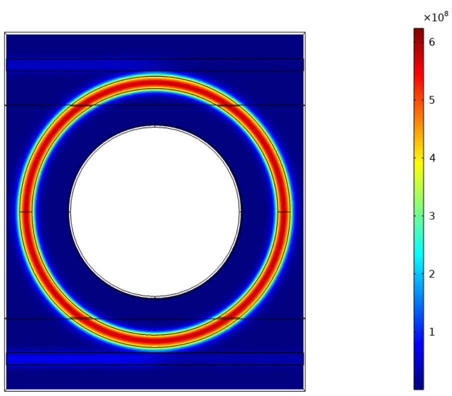

(a) normE on resonance.

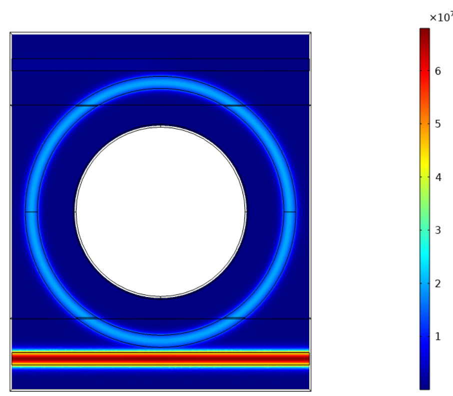

(b) normE off resonance.

Figure A.4: TE mode, 5 μm radius ring with an air cladding. Top-down, cross-sectional, 3D plots of the normE component on and off resonance.

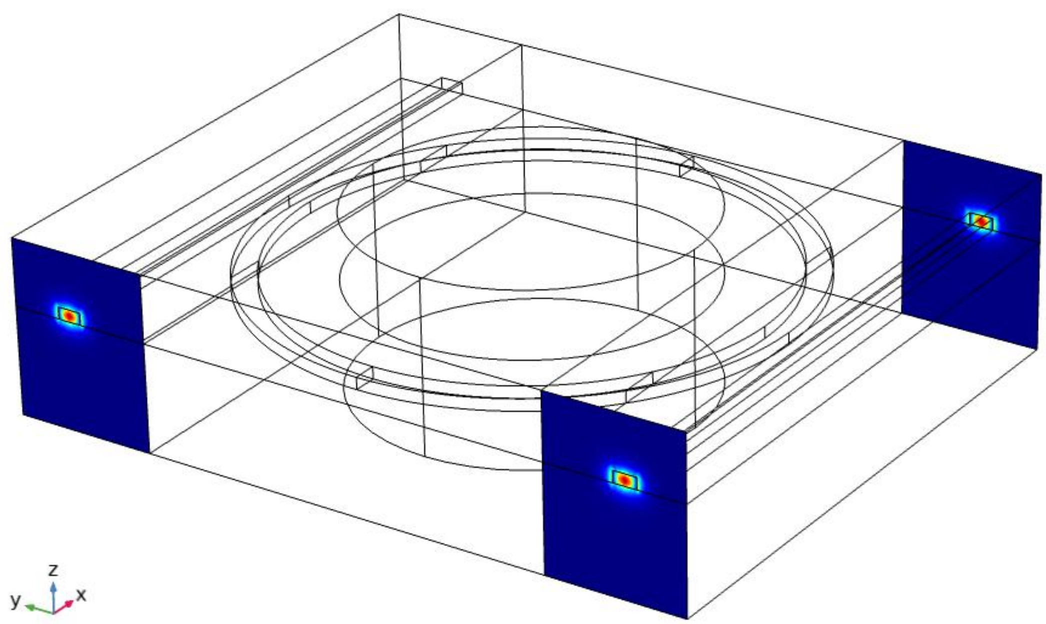

Figure A.5: Plot showing the BMA at each port on the 3D structure simultaneously. Left: Drop-port, Middle: Input, Right: Through-port

Bibliography

[1] L. Chrostowski, S. Grist, J. Flueckiger, W. Shi, X. Wang, E. Ouellet, H. Yun, M. Webb, B. Nie, Z. Liang, K. C. Cheung, S. A. Schmidt, D. M. Ratner, and N. A. F. Jaeger, "Silicon photonic resonator sensors and devices," (San Francisco, California, USA), p. 823620, Feb. 2012.

[2] N. Bhalla, P. Jolly, N. Formisano, and P. Estrela, "Introduction to biosensors," *Essays in Biochemistry*, vol. 60, pp. 1–8, June 2016.

[3] M. M. Ivancic, B. W. Megna, Y. Sverchkov, M. Craven, M. Reichelderfer, P. J. Pickhardt, M. R. Sussman, and G. D. Kennedy, "Noninvasive Detection of Colorectal Carcinomas Using Serum Protein Biomarkers," *The Journal of Surgical Research*, vol. 246, pp. 160–169, Feb. 2020.

[4] M. Bahadori, K. Bergman, M. Nikdast, S. Rumley, L. Y. Dai, N. Janosik, T. Van Vaerenbergh, A. Gazman, Q. Cheng, and R. Polster, "Design Space Exploration

of Microring Resonators in Silicon Photonic Interconnects: Impact of the Ring Curvature," *Journal of Lightwave Technology*, vol. 36, pp. 2767–2782, July 2018.

[5] Cadence System Analysis, "FDTD vs. FEM vs. MoM: What Are They and How Are They Different?," 2021.

[6] A. P. F. Turner, "Biosensors: sense and sensibility," *Chemical Society Reviews*, vol. 42, no. 8, p. 3184, 2013.

[7] M. C. Cardenosa-Rubio, H. M. Robison, and R. C. Bailey, "Recent advances in environmental and clinical analysis using microring resonator–based sensors," *Current Opinion in Environmental Science & Health*, vol. 10, pp. 38–46, Aug. 2019.

[8] W. J. Peveler, M. Yazdani, and V. M. Rotello, "Selectivity and Specificity: Pros and Cons in Sensing," *ACS Sensors*, vol. 1, pp. 1282–1285, Nov. 2016. Publisher: American Chemical Society.

[9] Madhukar Varshney and Kumar Mallikarjunan, "Challenges in Biosensor Development–Detection limit, detection time, and specificity," *Resource: Engineering and Technology for Sustainable World*, vol. 16, pp. 18–21, Oct. 2009.

[10] M. A. Morales and J. Mark Halpern, "Guide to Selecting a Biorecognition Element for Biosensors," *Bioconjugate chemistry*, vol. 29, pp. 3231–3239, Oct. 2018.

[11] N. De Acha, A. B. Socorro-Leránoz, C. Elosúa, and I. R. Matías, "Trends in the Design of Intensity-Based Optical Fiber Biosensors (2010–2020)," *Biosensors*, vol. 11, p. 197, June 2021. Number: 6 Publisher: Multidisciplinary Digital Publishing Institute.

[12] M. S. Nawrocka, T. Liu, X. Wang, and R. R. Panepucci, "Tunable silicon microring resonator with wide free spectral range," *Applied Physics Letters*, vol. 89, p. 071110, Aug. 2006. Publisher: American Institute of Physics.

[13] M. I. Cheema, C. Shi, A. M. Armani, and A. G. Kirk, "Optimizing the Signal to Noise Ratio of Microcavity Sensors," *IEEE Photonics Technology Letters*, vol. 26, pp. 2023–2026, Oct. 2014. Conference Name: IEEE Photonics Technology Letters.

[14] L. Nicu and T. Leïchlé, "Biosensors and tools for surface functionalization from the macro- to the nanoscale: The way forward," *Journal of Applied Physics*, vol. 104, p. 111101, Dec. 2008. Publisher: American Institute of Physics.

[15] V. Naresh and N. Lee, "A Review on Biosensors and Recent Development of Nanostructured Materials-Enabled Biosensors," *Sensors*, vol. 21, p. 1109, Jan. 2021. Number: 4 Publisher: Multidisciplinary Digital Publishing Institute.

[16] O. Parkash and R. H. Shueb, "Diagnosis of Dengue Infection Using Conventional and Biosensor Based Techniques," *Viruses*, vol. 7, pp. 5410–5427, Oct. 2015. Number: 10 Publisher: Multidisciplinary Digital Publishing Institute.

[17] Y. Y. Kong, C. H. Thay, T. C. Tin, and S. Devi, "Rapid detection, serotyping and quantitation of dengue viruses by TaqMan real-time one-step RT-PCR," *Journal of Virological Methods*, vol. 138, pp. 123–130, Dec. 2006.

[18] K. Lind and M. Kubista, "Development and evaluation of three real-time immuno-PCR assemblages for quantification of PSA," *Journal of Immunological Methods*, vol. 304, pp. 107–116, Sept. 2005.

[19] D. A. Healy, C. J. Hayes, P. Leonard, L. McKenna, and R. O'Kennedy, "Biosensor developments: application to prostate-specific antigen detection," *Trends in Biotechnology*, vol. 25, pp. 125–131, Mar. 2007.

[20] C. Cao, J. P. Kim, B. W. Kim, H. Chae, H. C. Yoon, S. S. Yang, and S. J. Sim, "A strategy for sensitivity and specificity enhancements in prostate specific antigen-1-antichymotrypsin detection based on surface plasmon resonance," *Biosensors and Bioelectronics*, vol. 21, pp. 2106–2113, May 2006.

[21] L. Huang, G. Reekmans, D. Saerens, J.-M. Friedt, F. Frederix, L. Francis, S. Muyldermans, A. Campitelli, and C. V. Hoof, "Prostate-specific antigen immunosensing based on mixed self-assembled monolayers, camel antibodies and colloidal gold enhanced sandwich assays," *Biosensors and Bioelectronics*, vol. 21, pp. 483–490, Sept. 2005.

[22] R. Franco-Duarte, S. Kadam, K. S. Kaushik, S. Painuli, P. Semwal, N. Cruz-Martins, and C. F. Rodrigues, “Chapter 59 - Quick detection and confirmation of microbes in food and water,” in *Present Knowledge in Food Safety* (M. E. Knowles, L. E. Anelich, A. R. Boobis, and B. Popping, eds.), pp. 893–916, Academic Press, Jan. 2023.

[23] Q. Zhao, D. Lu, G. Zhang, D. Zhang, and X. Shi, “Recent improvements in enzyme-linked immunosorbent assays based on nanomaterials,” *Talanta*, vol. 223, p. 121722, Feb. 2021.

[24] Thermo Fisher Scientific, “Overview of ELISA.”

[25] Bio-Techne, “Calculating the True Cost of ELISA.”

[26] Berthold Technologies GmbH & Co.KG, “ELISA Formats.”

[27] M. Alhajj, M. Zubair, and A. Farhana, “Enzyme Linked Immunosorbent Assay,” in *StatPearls*, Treasure Island (FL): StatPearls Publishing, 2023.

[28] M. K. Sezgintürk, “Chapter One - Introduction to commercial biosensors,” in *Commercial Biosensors and Their Applications* (M. K. Sezgintürk, ed.), pp. 1–28, Elsevier, Jan. 2020.

[29] A. J. Bandodkar, S. Imani, R. Nuñez-Flores, R. Kumar, C. Wang, A. M. Vinu Mohan, J. Wang, and P. P. Mercier, “Re-usable electrochemical glucose sensors integrated into a smartphone platform,” *Biosensors & bioelectronics*, vol. 101, pp. 181–187, Mar. 2018.

[30] L. S. Puumala, S. M. Grist, J. M. Morales, J. R. Bickford, L. Chrostowski, S. Shekhar, and K. C. Cheung, "Biofunctionalization of Multiplexed Silicon Photonic Biosensors," *Biosensors*, vol. 13, p. 53, Jan. 2023. Number: 1 Publisher: Multidisciplinary Digital Publishing Institute.

[31] C. Ciminelli, F. Dell'Olio, D. Conteduca, and M. N. Armenise, "Silicon photonic biosensors," *IET Optoelectronics*, vol. 13, no. 2, pp. 48–54, 2019. _eprint: https://onlinelibrary.wiley.com/doi/pdf/10.1049/iet-opt.2018.5082.

[32] E. Luan, H. Shoman, D. M. Ratner, K. C. Cheung, and L. Chrostowski, "Silicon Photonic Biosensors Using Label-Free Detection," *Sensors*, vol. 18, p. 3519, Oct. 2018. Number: 10 Publisher: Multidisciplinary Digital Publishing Institute.

[33] E. Valera, W. W. Shia, and R. C. Bailey, "Development and validation of an immunosensor for monocyte chemotactic protein 1 using a silicon photonic microring resonator biosensing platform," *Clinical Biochemistry*, vol. 49, pp. 121–126, Jan. 2016.

[34] M. S. Luchansky and R. C. Bailey, "Silicon Photonic Microring Resonators for Quantitative Cytokine Detection and T-Cell Secretion Analysis," *Analytical Chemistry*, vol. 82, pp. 1975–1981, Mar. 2010. Publisher: American Chemical Society.

[35] J. T. Kindt, M. S. Luchansky, A. J. Qavi, S.-H. Lee, and R. C. Bailey, "Subpicogram Per Milliliter Detection of Interleukins Using Silicon Photonic Microring Resonators and

an Enzymatic Signal Enhancement Strategy," *Analytical Chemistry*, vol. 85, pp. 10653–10657, Nov. 2013. Publisher: American Chemical Society.

[36] Y. Chen, Y. Liu, X. Shen, Z. Chang, L. Tang, W.-F. Dong, M. Li, and J.-J. He, "Ultrasensitive Detection of Testosterone Using Microring Resonator with Molecularly Imprinted Polymers," *Sensors*, vol. 15, pp. 31558–31565, Dec. 2015. Number: 12 Publisher: Multidisciplinary Digital Publishing Institute.

[37] H. M. Robison, P. Escalante, E. Valera, C. L. Erskine, L. Auvil, H. C. Sasieta, C. Bushell, M. Welge, and R. C. Bailey, "Precision immunoprofiling to reveal diagnostic signatures for latent tuberculosis infection and reactivation risk stratification," *Integrative Biology*, vol. 11, pp. 16–25, Jan. 2019.

[38] S. Dante, D. Duval, B. Sepúlveda, A. B. González-Guerrero, J. R. Sendra, and L. M. Lechuga, "All-optical phase modulation for integrated interferometric biosensors," *Optics Express*, vol. 20, pp. 7195–7205, Mar. 2012. Publisher: Optica Publishing Group.

[39] W. Bogaerts, P. De Heyn, T. Van Vaerenbergh, K. De Vos, S. Kumar Selvaraja, T. Claes, P. Dumon, P. Bienstman, D. Van Thourhout, and R. Baets, "Silicon microring resonators," *Laser & Photonics Reviews*, vol. 6, pp. 47–73, Jan. 2012.

[40] S. Schmidt, J. Flueckiger, W. Wu, S. M. Grist, S. T. Fard, V. Donzella, P. Khumwan, E. R. Thompson, Q. Wang, P. Kulik, X. Wang, A. Sherwali, J. Kirk, K. C. Cheung, L. Chrostowski, and D. Ratner, "Improving the performance of silicon photonic

rings, disks, and Bragg gratings for use in label-free biosensing," in *Biosensing and Nanomedicine VII*, vol. 9166, pp. 71–108, SPIE, Aug. 2014.

[41] H. P. Bazargani, J. Flueckiger, L. Chrostowski, and J. Azaña, "Microring resonator design with improved quality factors using quarter Bezier curves," in *2015 Conference on Lasers and Electro-Optics (CLEO)*, pp. 1–2, May 2015. ISSN: 2160-8989.

[42] V. R. Kolli and S. Talabattula, "An Optimized Integrated Optical Coupled Micro Ring Resonator for Low Pressure Sensing," *IEEE Sensors Journal*, vol. 22, pp. 16016–16026, Aug. 2022. Conference Name: IEEE Sensors Journal.

[43] L. Ali, M. U. Mohammed, M. Khan, A. H. B. Yousuf, and M. H. Chowdhury, "High-Quality Optical Ring Resonator-Based Biosensor for Cancer Detection," *IEEE Sensors Journal*, vol. 20, pp. 1867–1875, Feb. 2020. Conference Name: IEEE Sensors Journal.

[44] S. T. Fard, V. Donzella, S. A. Schmidt, J. Flueckiger, S. M. Grist, P. T. Fard, Y. Wu, R. J. Bojko, E. Kwok, N. A. F. Jaeger, D. M. Ratner, and L. Chrostowski, "Performance of ultra-thin SOI-based resonators for sensing applications," *Optics Express*, vol. 22, pp. 14166–14179, June 2014. Publisher: Optica Publishing Group.

[45] Jian-Ming Jin, "The Finite Element Method," in *Theory and Computation of Electromagnetic Fields*, pp. 342–398, John Wiley & Sons, Ltd, 2010. Section: 9 _eprint: https://onlinelibrary.wiley.com/doi/pdf/10.1002/9780470874257.ch9.

[46] K.-J. Bathe, "Finite Element Method," in *Wiley Encyclopedia of Computer Science and Engineering*, pp. 1–12, John Wiley & Sons, Ltd, 2008. _eprint: https://onlinelibrary.wiley.com/doi/pdf/10.1002/9780470050118.ecse159.

[47] K. McGarvey, "MANIPULATING STATES OF LIGHT IN OPTICAL RING RESONATORS,"

[48] M. Oheim, A. Salomon, A. Weissman, M. Brunstein, and U. Becherer, "Calibrating Evanescent-Wave Penetration Depths for Biological TIRF Microscopy," *Biophysical Journal*, vol. 117, pp. 795–809, Sept. 2019.

[49] H. H. Li, "Refractive index of silicon and germanium and its wavelength and temperature derivatives," *Journal of Physical and Chemical Reference Data*, vol. 9, pp. 561–658, July 1980.

[50] "Ring Resonators: Theory and Modeling," in *Integrated Ring Resonators: The Compendium* (D. G. Rabus, ed.), Springer Series in Optical Sciences, pp. 3–40, Berlin, Heidelberg: Springer, 2007.

[51] W. R. McKinnon, D.-X. Xu, C. Storey, E. Post, A. Densmore, A. Delâge, P. Waldron, J. H. Schmid, and S. Janz, "Extracting coupling and loss coefficients from a ring resonator," *Optics Express*, vol. 17, pp. 18971–18982, Oct. 2009. Publisher: Optica Publishing Group.

[52] T. Christopoulos, O. Tsilipakos, O. Tsilipakos, G. Sinatkas, and E. E. Kriezis, "On the calculation of the quality factor in contemporary photonic resonant structures," *Optics Express*, vol. 27, pp. 14505–14522, May 2019. Publisher: Optica Publishing Group.

[53] S. Talebi Fard, S. M. Grist, V. Donzella, S. A. Schmidt, J. Flueckiger, X. Wang, W. Shi, A. Millspaugh, M. Webb, D. M. Ratner, K. C. Cheung, and L. Chrostowski, "Label-free silicon photonic biosensors for use in clinical diagnostics," (San Francisco, California, USA), p. 862909, Mar. 2013.

[54] K. Qian, J. Tang, H. Guo, W. Liu, J. Liu, C. Xue, Y. Zheng, and C. Zhang, "Under-Coupling Whispering Gallery Mode Resonator Applied to Resonant Micro-Optic Gyroscope," *Sensors*, vol. 17, p. 100, Jan. 2017. Number: 1 Publisher: Multidisciplinary Digital Publishing Institute.

[55] J. Heebner, V. Wong, A. Schweinsberg, R. Boyd, and D. Jackson, "Optical transmission characteristics of fiber ring resonators," *IEEE Journal of Quantum Electronics*, vol. 40, pp. 726–730, June 2004. Conference Name: IEEE Journal of Quantum Electronics.

[56] B. Mou, Y. Boxia, Q. Yan, W. Yanwei, H. Zhe, Y. Fan, and W. Yu, "Ultrahigh Q SOI ring resonator with a strip waveguide," *Optics Communications*, vol. 505, p. 127437, Feb. 2022.

[57] S. M. Grist, S. A. Schmidt, J. Flueckiger, V. Donzella, W. Shi, S. T. Fard, J. T. Kirk, D. M. Ratner, K. C. Cheung, and L. Chrostowski, "Silicon photonic micro-disk

resonators for label-free biosensing," *Optics Express*, vol. 21, pp. 7994–8006, Apr. 2013. Publisher: Optica Publishing Group.

[58] A. Densmore, D.-X. Xu, P. Waldron, S. Janz, P. Cheben, J. Lapointe, A. Delage, B. Lamontagne, J. H. Schmid, and E. Post, "A Silicon-on-Insulator Photonic Wire Based Evanescent Field Sensor," *IEEE Photonics Technology Letters*, vol. 18, pp. 2520–2522, Dec. 2006. Conference Name: IEEE Photonics Technology Letters.

[59] B. Sepúlveda, G. Armelles, and L. M. Lechuga, "Magneto-optical phase modulation in integrated Mach–Zehnder interferometric sensors," *Sensors and Actuators A: Physical*, vol. 134, pp. 339–347, Mar. 2007.

[60] K. K. Lee, D. R. Lim, H.-C. Luan, A. Agarwal, J. Foresi, and L. C. Kimerling, "Effect of size and roughness on light transmission in a Si/SiO2 waveguide: Experiments and model," *Applied Physics Letters*, vol. 77, pp. 1617–1619, Sept. 2000.

[61] C. Qiu, Z. Sheng, H. Li, W. Liu, L. Li, A. Pang, A. Wu, X. Wang, S. Zou, and F. Gan, "Fabrication, Characterization and Loss Analysis of Silicon Nanowaveguides," *Journal of Lightwave Technology*, vol. 32, pp. 2303–2307, July 2014. Conference Name: Journal of Lightwave Technology.

[62] A. Prinzen, J. Bolten, M. Waldow, and H. Kurz, "Study on fabrication tolerances of SOI based directional couplers and ring resonators," *Microelectronic Engineering*, vol. 121, pp. 51–54, June 2014.

[63] A. Grosman, T. Duanis-Assaf, N. Mazurski, R. Zektzer, C. Frydendahl, L. Stern, M. Reches, and U. Levy, "On-chip multivariant COVID 19 photonic sensor based on silicon nitride double-microring resonators," *Nanophotonics*, vol. 12, pp. 2831–2839, July 2023. Publisher: De Gruyter.

[64] COMSOL, "Detailed Explanation of the Finite Element Method (FEM)," 2016.

[65] B. M. Irons, "Engineering applications of numerical integration in stiffness methods.," *AIAA Journal*, vol. 4, pp. 2035–2037, Nov. 1966. Publisher: American Institute of Aeronautics and Astronautics.

[66] COMSOL Multiphysics Team, "Wave Optics Module User's Guide," 2021.

[67] E. Hecht, *Optics*. Pearson Education, Inc., 5 ed., Jan. 2017. Publication Title: Optics ADS Bibcode: 2017opti.book.....H.

[68] J. Flueckiger, S. Schmidt, V. Donzella, A. Sherwali, D. M. Ratner, L. Chrostowski, and K. C. Cheung, "Sub-wavelength grating for enhanced ring resonator biosensor," *Optics Express*, vol. 24, pp. 15672–15686, July 2016. Publisher: Optica Publishing Group.

[69] CMC Microsystems, "Applied Nanotools (ANT) NanoSOI Fabrication Process – CMC Microsystems."

[70] W. Bogaerts, V. Wiaux, D. Taillaert, S. Beckx, B. Luyssaert, P. Bienstman, and R. Baets, "Fabrication of photonic crystals in silicon-on-insulator using 248-nm deep

UV lithography," *IEEE Journal of Selected Topics in Quantum Electronics*, vol. 8, pp. 928–934, July 2002. Conference Name: IEEE Journal of Selected Topics in Quantum Electronics.

[71] N. A. Yebo, S. P. Sree, E. Levrau, C. Detavernier, Z. Hens, J. A. Martens, and R. Baets, "Selective and reversible ammonia gas detection with nanoporous film functionalized silicon photonic micro-ring resonator," *Optics Express*, vol. 20, pp. 11855–11862, May 2012. Publisher: Optica Publishing Group.

[72] K. D. Vos, I. Bartolozzi, E. Schacht, P. Bienstman, and R. Baets, "Silicon-on-Insulator microring resonator for sensitive and label-free biosensing," *Optics Express*, vol. 15, pp. 7610–7615, June 2007. Publisher: Optica Publishing Group.

[73] Applied Nanotools Inc., "NanoSOI Fabrication Service | Applied Nanotools Inc.," Mar. 2020.

[74] S. Kedenburg, M. Vieweg, T. Gissibl, and H. Giessen, "Linear refractive index and absorption measurements of nonlinear optical liquids in the visible and near-infrared spectral region," *Optical Materials Express*, vol. 2, pp. 1588–1611, Nov. 2012. Publisher: Optica Publishing Group.

[75] I. H. Malitson, "Interspecimen Comparison of the Refractive Index of Fused Silica*,†," *JOSA*, vol. 55, pp. 1205–1209, Oct. 1965. Publisher: Optica Publishing Group.

[76] E. R. Peck and K. Reeder, “Dispersion of Air*,” *JOSA*, vol. 62, pp. 958–962, Aug. 1972. Publisher: Optica Publishing Group.